Estrogen Receptor Alpha Somatic Mutations Y537S and D538G Confer Breast Cancer Endocrine Resistance by Stabilizing the Activating Function-2 Binding Conformation

Sean W. Fanning[1*], Christopher G. Mayne[2,5*], Venkatasubramanian Dharmarajan[3*], Kathryn E. Carlson[2], Teresa A. Martin[2], Scott J. Novick[3], Weiyi Toy[4], Bradley Green[1], Srinivas Panchamukhi[1], Benita S. Katzenellenbogen[6], Emad Tajkhorshid[5], Patrick R. Griffin[3], Yang Shen[7], Sarat Chandarlapaty[4], John A. Katzenellenbogen[2], Geoffrey L. Greene[1+]

1: Ben May Department for Cancer Research, University of Chicago, Chicago, IL 60637 USA

2: Department of Chemistry, University of Illinois at Urbana-Champaign, Urbana, IL 61801 USA

3: Department of Molecular Therapeutics, The Scripps Research Institute, Jupiter, FL, 33458 USA

4: Human Oncology and Pathogenesis Program, Memorial Sloan Kettering Cancer Center (MSKCC), New York, NY 10065, USA

5: Department of Biochemistry, Center for Biophysics and Computational Biology, and Beckman Institute for Advanced Science and Technology, University of Illinois at Urbana-Champaign, Urbana, IL, 61801 USA

6: Department of Molecular and Integrative Physiology, University of Illinois at Urbana-Champaign, Urbana, IL 61801 USA

7: Department of Electrical and Computer Engineering, Center for Bioinformatics and Genomic Systems Engineering, Texas A&M University, College Station, TX 77843 USA

*Indicates equal contributions.

[+]Corresponding Author: Geoffrey L. Greene, Ph.D., Ben May Department for Cancer Research, University of Chicago, Chicago, IL 60637. Email: ggreene@uchicago.edu

Abstract

Somatic mutations in the estrogen receptor alpha (ERα) gene (*ESR1*), especially Y537S and D538G, have been linked to acquired resistance to endocrine therapies. Cell based studies demonstrated that these mutants confer ERα constitutive activity and antiestrogen resistance and suggest that ligand-binding domain dysfunction leads to endocrine therapy resistance. Here, we integrate biophysical and structural biology data to reveal how these mutations lead to a constitutively active and antiestrogen resistant ERα. We show that these mutant ERs recruit coactivator in the absence of hormone while their affinities for estrogen agonist (estradiol) and antagonist (4-hydroxytamoxifen) are reduced. Further, they confer antiestrogen resistance by altering the conformational dynamics of the loop connecting Helix 11 and Helix 12 in the ligand-binding domain of ERα, which leads to a stabilized agonist state and an altered antagonist state that resists inhibition.

Introduction

The estrogen receptor α (ERα) is a ligand-activated nuclear hormone receptor and a major regulator of cell growth, survival and metastasis in a large fraction of breast cancers. Inhibiting the action of ERα with selective estrogen receptor modulators (SERMs) or selective estrogen receptor degraders (SERDs), or reducing endogenous estrogen levels with aromatase inhibitors (AI), are effective treatments for many of these breast cancers (Strasser-Weippl and Goss, 2005). Due to their efficacy and broad therapeutic indices, antiestrogens can be administered sequentially for progressive disease over the course of several years (Toy et al., 2013). Unfortunately, despite continued expression of ERα, the majority of metastatic breast cancers that initially respond to endocrine therapies become refractory.

Recently, somatic mutations in the ERα gene (*ESR1*) were linked to acquired resistance to endocrine therapies of breast cancer (Toy et al., 2013; Merenbakh-Lamin et al., 2013; Robinson et al., 2013; Li et al., 2014; Jeselsohn et al., 2014). Approximately 25% of patients who previously received SERM/SERD/AI treatments for an average of 5 years presented with conserved somatic mutations that were not identified in primary (untreated) tumors. The most prevalent ERα point mutations were Y537S and D538G, while several others were identified at significantly reduced frequencies. Importantly, breast cancer cell based studies revealed that the Y537S and D538G mutations conferred hormone-independent activation of ERα and reduced the inhibitory potency and efficacy of clinically prescribed SERMs and SERDs (Toy et al., 2013; Merenbakh-Lamin et al., 2013; Robinson et al., 2013; Li et al., 2014; Jeselsohn et al., 2014; Carlson et al., 1997). Notably, the constitutive activity and antagonist resistance of the Y537S and E380Q mutations were first described in cell models in 1996 (Weis et al.,1996), and shortly thereafter the Y537N mutation was found in a clinical sample of metastatic breast cancer (Zhang et al., 1997). However, no clinical follow up studies were reported until 2013.

The Y537S and D538G mutations are especially interesting because they occur at the N-terminus of Helix 12 (H12) in the ERα ligand-binding domain (LBD). Structurally, ERα LBD is an α-helical bundle, with the C-terminal helix, H12, functioning as a key structural component of the activating function-2

(AF-2) cleft that governs the agonist or antagonist state of the receptor. In the agonist conformation (*e.g.,* estradiol (E2)-bound), H12 covers the ligand binding pocket, docking between Helices 3 (H3) and 11 (H11), thereby facilitating coactivator recruitment to the AF-2 cleft via canonical LXXLL coactivator sequence motifs. In contrast, in the antagonist state (*e.g.,* SERM-bound), H12 occupies the AF-2 cleft using its own LXXML sequence, thereby blocking coactivator recruitment and ERα action.

In this study, biophysical assays reveal the impact of the Y537S and D538G mutations on ERα LBD ligand and co-regulator binding affinity. Additionally, x-ray crystal structures and atomistic molecular dynamics (MD) simulations uncover altered conformations adopted by the mutant receptors in the absence and presence of agonists and antagonists. Together, these findings present a molecular explanation for how the Y537S and D538G mutations elevate the basal or constitutive activity of ERα and confer resistance to the beneficial effects of the SERM, SERD, and AI therapies. A comprehensive understanding of how these and other gain-of-function mutations alter the structure and function of ERα is crucial to development of more efficacious and potent inhibitors to target these mutant receptors in the clinic.

Results

Y537S and D538G Promote Constitutive Coactivator Binding to ERα

An established time-resolved Förster Resonance Energy Transfer (tr-FRET) assay that determines the affinity of the steroid receptor coactivator 3 nuclear receptor domain (SRC3 NRD) for the ERs was used to investigate differences among the WT, Y537S, and D538G (Tamrazi et al., 2005, Jeyakumar et al., 2011). SRC3 was chosen because of its abundance in breast cancer cells and high affinity for ERα (Liao et al., 2002). **Table 1** summarizes all SRC3 coactivator binding affinities. SRC3 NRD bound to the E2-saturated WT ERα LBD with high affinity (K_d = 2.67 ± 0.5 nM) while no binding was detected in the absence of E2 or in the presence of the SERM 4-hydroxytamoxifen (TOT; the active metabolite of tamoxifen) (**Figure 1**). In contrast, the SRC3 NRD bound to Y537S and D538G ERα in the absence of E2, with affinities of 13.6 ± 2.0 nM and 151 ± 20 nM, respectively, and the binding curves reached

87 approximately 60% of the maximum (**Figure 1**). When Y537S and D538G were pre-saturated with E2,
88 the SRC3 binding curves reached the same maximum as WT with E2, with the coactivator binding
89 affinity for the mutants being comparable or slightly higher than WT (WT EC_{50} = 2.67 ± 0.5 nM; Y537S
90 = 0.59 ± 0.1 nM; D538G = 3.65 ± 0.4 nM) (**Figure 1**). Neither the WT nor the mutants bound coactivator
91 when pre-incubated with saturating concentrations TOT (**Figure 1**).

92 To determine the potency of ligands to affect coactivator binding to the ER, ligand was titrated into a
93 constant amount of SRC3 and ER and measured by tr-FRET. Addition of E2 resulted in increased
94 coactivator affinity to the Y537S (EC_{50} = 1.6 ± 1.2 nM) and D538G (EC_{50} = 2.2 ± 0.1 nM) ERα LBD.
95 Interestingly, the EC_{50} value was somewhat reduced for WT (EC_{50} = 13.8 ± 0.9 nM) (**Figure 1-figure**
96 **supplement 1**). TOT abolished basal Y537S and D538G SRC3 binding in the absence of agonist. To
97 mimic this reversal in WT, which does not bind SRC3 NRD without ligand, a low concentration of E2
98 was added to WT-ER to recruit SRC3 NRD to about 50% of maximal (data not shown). As expected,
99 titration of TOT reversed the binding of SRC3 NRD by the mutant ER and E2-primed WT. The EC_{50}
100 values for suppressing SRC3 binding of the mutant (done in the absence of agonist) were comparable to
101 the K_i values for WT. The K_i of TOT was 1.82 ± 0.30 nM for WT, 6.7 ± 0.40 nM for Y537S, and 0.79 ±
102 0.04 nM for D538G.

103 **The Y537S and D538G Mutants Bind Ligands with Reduced Affinity**

104 Our earlier work demonstrated that SERMs were less potent in inhibiting the transcriptional activity
105 of the ERα Y537S and D538G mutants compared to WT in breast cancer cells (Toy et al., 2013). The
106 binding affinities of E2 with the WT and mutant ERα LBDs were measured using radioligand-binding
107 assays (Carlson et al., 1997). The affinity of E2 for WT-ER (K_d = 0.26 ± 0.13 nM) is approximately 5-
108 fold greater than for the mutants, Y537S (K_d = 1.43 ± 0.55 nM) and D538G (K_d = 1.30 ± 0.63 nM)
109 (**Figure 2**). **Table 2** summarizes all ligand binding affinities for the WT and mutant ERα LBDs.

110 A competitive radioligand-binding assay with ^{3}H-E2 as tracer was used to measure the relative
111 competitive binding affinities (RBAs) of TOT for WT and the mutant-ERs (Katzenellenbogen et al.,

1973; Carlson et al., 1997). The K_i of TOT binding to WT was 0.337 ± 0.018 nM, whereas it was 2.61 ± 0.60 nM and 3.42 ± 0.5 nM for the Y537S and D538G mutants, respectively. Comparing the K_i values, it is notable that the affinity of TOT for the Y537S and D538G mutants is impaired approximately 8- and 10-fold relative to WT (**Table 2**). This reduced binding affinity is consistent with the published lower inhibitory potency of TOT on the mutants in breast cancer cells (Toy et al., 2013). **Figure 3** shows representative radiometric competitive binding measurements.

Biophysical Basis for Aberrant Coregulator Recruitment by Y537S and D538G ERα LBD Mutants

Proteolytic Susceptibility – An established trypsin digestion assay was used to determine whether the conformational dynamics of the LBD H11-12 loop and H12 are altered as a result of the Y537S and D538G mutations (Tamrazi et al. 2003). The measured half-life for H11-12 loop and H12 cleavage ($t_{1/2}$) of the unliganded (*apo*) WT ERα LBD was 2 minutes, indicating that this region is highly mobile (**Figure 4A**). In contrast, the H11-12 loop and H12 region displayed significantly reduced proteolysis for *apo* D538G, with a $t_{1/2}$ of 19 minutes. A further reduction was observed for the H11-12 loop and H12 for *apo* Y537S with a $t_{1/2}$ = 87 minutes. When incubated with saturating concentrations of E2, each of the LBDs displayed increased stability of the H11-12 loop and H12 with $t_{1/2}$ = 5 minutes for the WT, 140 minutes for Y537S, and no detectible cleavage for D538G (**Figure 4A**). This lack of proteolysis for the D538G-E2 complex suggests that the H11-12 loop and H12 are stabilized and in a conformation that resists trypsin proteolysis. Importantly, the trend of H11-12 loop and H12 mobility observed for *apo* LBDs correlates with the relative coactivator binding affinities for *apo* WT and mutant LBDs as the Y537S mutant is the least dynamic and has the highest affinity for the coregulator.

Hydrogen/Deuterium Exchange Mass Spectrometry **–** Hydrogen/deuterium exchange mass spectrometry (HDX-MS) was used to further dissect the consequences of Y537S and D538G ERα LBD mutations on the conformational mobility of the H11-12 loop and H12. Perturbation in time-dependent deuterium uptake profiles (measured as protection to number of exchanged amide hydrogens with solvent

deuterium between two states) is indicative of conformational alterations due to rearrangement of amide hydrogen bonds (Horn et al. 2006). Differential amide HDX experiments were performed to compare the conformational dynamics of liganded and unliganded (*apo*) receptors. H11, the H11-12 loop, and H12 were all protected from solvent exchange for WT, D538G and Y537S ERα LBD in the presence of E2 as compared to *apo* receptor (solvent exchange was lower for peptides containing these structural elements in the presence of ligand as compared to unliganded receptor), indicating the adoption of a more stable agonist-bound conformation matching that observed in x-ray co-crystal structures (**Figure 4B, 4C, and Figure 4-figure supplements 1-3**). For the unliganded states, the H12 of Y537S and D538G exhibited increased solvent exchange (deprotection indicative of increased conformational dynamics) compared to WT ERα, suggesting that the mutant receptors adopt an alternative H12 conformation in the absence of E2. **Figure 4B-C** shows differential deuterium incorporation for the WT versus mutant ERα LBD in the *apo* states focusing on the H11-12 loop and H12 regions. **Figure 4-figure supplements 4 and 5** show the complete differential HDX perturbation maps comparing the *apo* WT versus *apo* Y537S and D538G ERα LBD, respectively. Interestingly, residues close in space to or within the AF-2 cleft (positions 310-325, 344-349, 370-380, and 405-410) of the *apo* Y537S also showed statistically significant increase in solvent exchange compared to *apo* WT. Similar deprotection was observed in residues 310-325 of the *apo* D538G. Together, the HDX data suggests that the Y537S and D538G mutants enables H12 to sample a suite of conformations that expose the AF-2 cleft at a greater frequency thereby facilitating coregulator recruitment in the absence of hormone. Furthermore, these data suggest that the Y537S mutant possesses a higher affinity for SRC3 as compared to D538G as it samples more frequently AF-2-cleft conformers that facilitate coregulator binding, in agreement with our *in vitro* SRC3 NRD binding experiments.

In order to test our hypothesis that the increased deuterium uptake in the H12 region of the mutants was due to a rearrangement of amide hydrogen bonds that could facilitate coactivator recruitment, we performed differential HDX analysis for the WT, Y537S and D538G ERα LBDs in the presence of SRC3 NRD, in the presence and absence of E2. Few statistically significant differences in solvent exchange

were observed in the C-terminus of LBD when the WT ERα LBD was incubated with saturating concentrations of SRC3 NRD, with the exception of H11 (**Figure 4-figure supplement 6**). In contrast, the H11-12 loop showed statistically significant protection from exchange in the Y537S-SRC3 NRD complex, indicating that the region in the Y537S mutant was further stabilized by the inclusion of coregulator (**Figure 4-figure supplement 7**). These results suggest that H12 in the *apo* mutant receptor is in a more favorable conformation promoting co-activator binding when compared to *apo* WT. The magnitude of protection from solvent exchange observed in the AF-2 cleft in Y537S with SRC3 NRD was further increased upon addition of E2 indicating a more stable Y537S-SRC3-E2 complex (**Figure 4-figure supplement 10**). In contrast to Y537S, the H11-12 loop and H12 in the D538G mutant did not show a statistically significant difference in deuterium incorporation in the presence of SRC3 NRD alone, but did show increased protection from solvent exchange in these regions in the presence of E2 (**Figure 4-figure supplements 8 and 10**). This finding could be attributed to the low intrinsic SRC3 NRD binding affinity of *apo* D538G as compared to Y537S (**Table 1**). Together, these data, along with the SRC3 NRD recruitment and trypsin susceptibility, suggest that the increased solvent exchange in H12 and AF-2 cleft residues for the *apo* Y537S is due to an altered conformation of H12 that promotes coactivator recruitment. This observation is apparent in the x-ray crystal structure of the *apo* Y537S. When compared to the WT-E2 complex (PDB: 1GWR), the serine at residue 537 in the *apo* Y537S (PDB: 2B23) replaces the phenolic side chain of WT Y537, exposing a solvent channel between the H11-12 loop and H3. Further, H12 is slightly displaced away from the ligand binding pocket towards solvent (**Figure 4-figure supplement 12**). It is important to note that the HDX MS studies provide novel insight into the conformational mobility of the WT H12, in that this helix does not reach maximum structural stability until both hormone and coregulator are bound.

Structural Basis for H12 Mutant Hormone-Independent Activity

X-ray Crystallographic Analysis of the D538G Agonist States - High resolution x-ray crystal structures of the *apo* and agonist-bound states of the Y537S, obtained earlier, revealed near identical H12

conformations, in which S537 formed a hydrogen bond with D351 to adopt a stable agonist state in the absence of hormone (Nettles et al., 2008). In this study, we obtained x-ray crystal structures for the D538G mutant bound to E2, without added ligand (*apo*), and bound to a SERM (4-hydroxytamoxifen).

D538G Mutation Induces Pronounced Conformational Changes in the Agonist Binding Mode – The D538G-E2 complex structure was solved to 1.90 Å resolution by molecular replacement, with one dimer in the asymmetric unit (ASU). All crystallographic statistics are reported in **Table 3**. Overall, the structure presents a canonical ERα LBD-agonist binding state where H12 covers the ligand-binding pocket situated between H3 and H11, and the GRIP peptide occupies the AF-2 cleft. The E2 ligand, GRIP peptide, and H12 (until residue L549) are well resolved in the map (**Figure 5-figure supplement 1**). No differences are observed in the residues comprising the ligand-binding pocket between the D538G-E2 and WT-E2 structures (Gangloff et al., 2001; Eiler et al., 2001; Phillips et al., 2011).

Pronounced conformational changes are observed in the loop connecting H11 and H12 (H11-12 loop, residues 531-537) in both monomers in the ASU for the D538G-E2 structure compared to the WT-E2 structure, although no appreciable changes are observed in most of H12. The H11-12 loop is displaced away from H3 and towards H11, accompanied by conformational changes in Y537 (**Figure 5**). In the WT-E2 structure, Y537 forms a hydrogen bond with N348 on H3, packing the H11-12 loop into the interior of the protein. In the D538G-E2 structure, however, the Y537 loses its hydrogen bond with N348, and its phenolic side chain is pointed towards bulk solvent. The space previously occupied by Y537 in WT is replaced by a well ordered water molecule in the mutant (observed in both monomers), which hydrogen bonds with the backbone amide of Y537 in between H3 and H12 (**Figure 5-figure supplement 2**). While the side chain orientations are identical for residues 531-536 between both monomers in the ASU, the side chain of Y537 appears to adopt two different conformations, both facing solvent, while the main chain orientation of Y537 is identical in the two monomers. It should be noted that the phenolic oxygen of Y537 maintains the same hydrogen bond to N348 in every WT ERα LBD-agonist structure available in the PDB. Thus, this rotation of Y537 is unique to the D538G-E2 structure, and it brings the φ

and ψ angles of residues 537 and 538 out of the α-helix region and into the allowed, more sheet-like region around -120° and 60° (defined by φ/ψ angle regions in the Ramachandran plot) (Ramachandran et al., 1963). In the resulting conformation, the α-helix of H12 begins at position 539 for the D538G-E2 structure rather than at 537 for the WT-agonist structures.

Few differences are observed between the unliganded and E2-bound D538G (C_α r.m.s.d. = 0.327 Å). The greatest conformational discrepancy between the two structures lies at Y537, which, in the unliganded structure, adopts a more WT-E2 like conformation by orienting towards H3 in chain A, thus returning the φ and ψ angles of residues 537 and 538 into the α-helical region. Y537 of chain B, however, matches the solvent-exposed orientation of the D538G-E2 structure whereby the φ and ψ angles for 537 and 538 are outside of the α-helical region. Based on this conformational asymmetry between the two monomers in *apo*-D538G ERα, Y537 can switch between the buried state observed in the WT-agonist structures and the solvent-exposed orientation of the D538G-E2 structure (**Figure 5-figure supplement 2A and B**). Thus, *apo* D538G has lost some—but not all—of the conformational attributes of the E2-bound mutant, which is consistent with its modest level of constitutive activity. Together, these structural features agree with our biophysical data showing that D538G can adopt an agonist state in the absence of hormone that recruits coregulator with a modest affinity.

It is of interest that the electron density map of *apo* D538G revealed some density in the ligand binding pocket representing a non-specific small molecule likely acquired during the expression of the protein, which remained during crystallization (**Figure 5-figure supplement 3**). A similar electron density was observed in the published *apo* Y537S (Nettles et al., 2008). The unidentified ligand is not of sufficient size to be a hormone nor is it near enough to H11 and H12 to interact with them. We believe that the unidentified small molecule in the ligand binding site is an artifact of protein expression in bacteria, as reported earlier for the Y537S structure, and does not influence H11 and H12 nor the loop connecting them (Nettles et al., 2008).

The Dynamics of D538G-Mediated Alterations of the H11-12 Loop– The previously published *apo* Y537S structure showed that S537 forms a hydrogen bond with D351 to adopt the agonist state in the absence of hormone thereby providing a clear conformational explanation for its constitutive activity (Nettles et al., 2008). In contrast, the *apo* D538G structure shows that this mutant may use a subtler mechanism to adopt the agonist conformation in the absence of hormone. In order to gain a better understanding of how the D538G mutation stabilizes the ERα LBD agonist conformation, MD simulations were performed on this mutant in the absence of ligand, and for WT ER (**Figure 6A**) in both the presence and absence of ligand. As was noted earlier, it has not been possible to obtain crystal structures of *apo* WT ER. Thus, to gain insights into the *apo* WT ERα LBD, MD simulations were performed by removing E2 from the ER complex prior to the dynamics run.

MD simulations of the WT and the D538G mutant showed an increased flexibility of the H11-12 loop as a result of the D538G mutation, inducing the Y537 side chain to rotate towards the bulk solvent (**Figure 6B**). This rotation shifts the backbone conformations of residues 535-537 (**Figure 6E**) to occupy regions of the Ramachandran plot that are similar to WT-E2 and distinct from *apo*-WT. These mutation-induced changes allow the H11-12 loop to adopt conformations similar to WT-E2, despite the absence of ligand. Computing the density maps for the side chain atoms of hydrophobic residues V533, V534, P535, and L536 further confirmed this altered state in which the resulting backbone conformation also permits new side chain positions (**Figure 6C, D**). Analysis of the averaged atomic density for residues 533-536 in the WT simulations reveals that the removal of the ligand (WT-E2 vs. *apo* WT, **Figure 6C**) results in more exposed positions for the hydrophobic residues in the loop region, thus destabilizing the H11-12 loop, while the D538G mutation allows the receptor to maintain side chain positions buried more deeply into the protein surface (WT-E2 vs. *apo* D538G, **Figure 6D**). Further, reduced fluctuations were exhibited in the WT-E2 and *apo*-D538G MD simulations, as observed from larger volumes for the given isosurface, thus indicating that the residues pack more favorably. The optimized packing of the hydrophobic loop residues was additionally quantified by the decreased solvent exposure for the WT-E2 and *apo* D538G

conformations compared to *apo* WT over the course of the entire simulation (**Figure 6F**). All of the changes that result from replacing D538 with glycine are consistent with increased stability of the H11-12 loop in the mutant, which likely contributes to its constitutive activity.

Structural and Biophysical Basis for Reduced SERM Potency

Trypsin Susceptibility of the H12 Mutants with TOT – Trypsin susceptibility was used to determine whether the antagonist state dynamics of the H11-12 loop and H12 were altered as a result of Y537S or D538G mutation. Interestingly, these regions showed decreased dynamics (*i.e.,* increased stability) for the Y537S and D538G mutants, which displayed $t_{1/2}$ = 60 and 62 minutes respectively, whereas the $t_{1/2}$ for the WT was 18 minutes (**Figure 4A**). These half-lives were higher than *apo* proteins alone suggesting that TOT binds and increases the overall stability of the protein (**Figure 4A**), though to a lesser extent than does E2.

HDX MS of the WT and Mutants in Complex with TOT- HDX MS was employed to probe the sequence specific conformational mobility of the Y537S and D538G antagonist states compared to the WT. Comparison of HDX profiles for TOT-bound WT and mutants revealed that the mutant proteins adopt alternate conformations in H11/12 regions relative to the WT complex (**Figure 7C-E**). **Figure 7-figure supplements 1-3** show deuterium uptake plots for the WT and mutant ERα LBDs in complex with TOT for the full protein sequence. Additionally, **Figure 7-figure supplements 4-6** show side-by-side comparisons for the WT, Y537S and D538G ERα LBD in complex with ligand and/or SRC3 NRD versus their individual *apo* states.

Structure of the D538G-TOT Complex - To explore the structural basis for reduced SERM potency and efficacy, the D538G mutant ERα LBD was co-crystallized with TOT. We were unable to obtain diffraction-quality crystals for Y537S in complex with any SERM. However, the D538G-TOT structure was solved to 3.06 Å with 4 dimers in the ASU by molecular replacement. The TOT ligand and H12 are both well resolved in every monomer (**Figure 5-figure supplement 1B**). Significant conformational differences are observed between WT-TOT (PDB: 3ERT) and D538G-TOT structures, both in H12 and

the H11-12 loop regions. We believe that these differences help account for the reduced potency and efficacy of TOT towards the D538G mutant ERα in breast cancer reporter gene assays.

As with the WT-TOT structure, H12 of the D538G-TOT structure lies in the AF-2 cleft; the conformation of H12 in the mutant structure, however, is altered compared to the WT (**Figure 7A**). In D538G-TOT, L536 is oriented towards solvent rather than docking into the well-defined leucine-binding pocket found in the WT-TOT structure, and P535 occupies the space previously occupied by the L536 of the WT (**Figure 7A**). The largest conformational change occurs in the H11-12 loop (residues 527-537). Instead of extruding towards solvent, the loop is packed towards the interior of the protein by 9.6 Å compared to the WT (V534 alpha carbon to alpha carbon) (**Figure 7A**). This conformational change likely explains why trypsin displayed a reduced ability to cleave at this region. Additionally, the tertiary amine at the terminus of the TOT ligand is observed in several conformations in the complex with D538G ER rather than the single conformation present in the WT-TOT structure. Together, these observations suggest that the flexibility of a glycine at position 538 reduces the ability of an antagonist to influence the H11-12 loop and H12. However, care must be taken when interpreting differences within this loop between the WT and the D538G mutant crystal structures. A crystal contact is formed in the WT-TOT structure between the backbone amide of K531 with the backbone carbonyl oxygen of K492 in a symmetry mate. Together, these data reveal that the D538G mutant adopts an altered antagonist conformation that resists antagonism relative to the WT-TOT complex.

Modeled Structure of the Y537S-TOT Complex - MD simulation was used to model Y537S with TOT because we were unable to obtain diffraction quality crystals for the complex. During the simulation, H12 of Y537S was found to lie within the AF-2 cleft in a perturbed conformation compared to the WT-TOT crystal structure, similar to that seen in the D538G-TOT crystal structure. Specifically, L536 no longer packs well with the leucine binding site on H3 but reorients to face the solvent, and the rest of the motif is also pushed outward and even shifted towards the C-terminus along the axial direction of H12 by half a turn (**Figure 7B**). These findings suggest that Y537S stabilizes H12 inside the AF-2

through the formation of a newly formed hydrogen bond (**Figure 7B**) that is predicted to form between S537 and E380. Like the D538G-TOT complex, our data for the Y537S-TOT complex show that these conformational changes serve to reduce the inhibitory potency of the SERM relative to the WT ERα LBD.

Discussion

Acquired resistance to endocrine therapies represents a substantial barrier towards obtaining prolonged remission of ER-dependent metastatic breast cancers for a significant population of patients. While somatic mutations in the androgen receptor are a known mechanism of acquired hormone therapy resistance in prostate cancer, somatic mutations in *ESR1* have only recently been identified as an important mechanism of acquired endocrine therapy resistance in breast cancer. Subsequent studies have established Y537S and D538G as the two most common point mutations conferring hormone-independent activation and reduced SERM/SERD/AI inhibitory potency and likely efficacy (Robinson et al., 2013; Toy et al., 2013; Jeselsohn et al., 2014). The clinical importance of these *ESR1* mutations highlights the importance of understanding the mechanisms by which they influence ERα structure and function.

Here, biochemical and biophysical techniques combined with x-ray crystal structures, and MD simulations provide a molecular explanation for how the Y537S and D538G point mutations in the ERα LBD alter the structure and function of the receptor. Coactivator binding assays show that these mutant LBDs recruit the SRC3 coactivator in the absence of hormone, while the unliganded WT LBD does not. Importantly, *apo* Y537S binds SRC3 NRD with a significantly increased affinity compared to D538G. This differential coactivator binding affinity likely accounts for the significantly increased constitutive transcriptional activity of Y537S vs. D538G in breast cancer cell line reporter gene assays (Toy et al., 2013). **Figure 8** shows a model for aberrant ERα activity as a result of Y537S and D538G mutations in the recurrent anti-estrogen resistant breast cancer cell. Ligand-binding assays demonstrate that both mutants possess a slightly reduced affinity for E2 and a significantly reduced affinity for TOT. Collectively, these data suggest that the combination of a recruitment of coactivator in the absence of hormone and a reduced TOT binding affinity underlie the hormone therapy resistance conferred by these H12 ERα mutations.

Comprehensive biophysical and structural investigations by proteolytic susceptibility assays, HDX-MS, x-ray crystallography, and MD simulations reveal how the Y537S and D538G mutations affect ERα in the *apo*, agonist, and antagonist-bound states, thereby providing a detailed structural explanation for the hormone-resistance conferred to the ERα. The Y537S and D538G mutations are located at or near H12, a key molecular switch governing the ligand-regulated actions of ERα via AF-2. Previously published *apo* and agonist-bound Y537S structures showed that S537 promotes the agonist conformation in the absence of ligand by forming a hydrogen bond to D351 (Nettles et al., 2008), in the process facilitating a tighter packing of the H11-12 loop against the LBD. Similarly, our analysis of the agonist-bound and *apo* D538G structures show that this mutation relaxes the helical character at the start of H12, thereby also relaxing the H11-12 loop and improving the packing of its hydrophobic side chains. Importantly, our data also show that binding of coregulator (SRC3) further stabilizes H12 in the agonist conformation. While the Y537S and D538G mutants may work through different mechanisms, both stabilize the agonist state in the absence of hormone. The D538G mutation, however, appears to be less stabilizing, as reflected by the lower constitutive activity of D538G ERα in both biochemical and cell-based assays (Toy et al., 2013).

Examination of the molecular basis for reduced SERM potency and efficacy for mutant ERα LBDs reveals that this likely evolves from structural changes to the H11-12 loop, resulting in a decreased binding affinity of antagonist ligands and an altered, stabilized, antagonist conformation of H12 in the AF-2 cleft. Our biophysical studies indicate that the H11-12 loop and H12 are both altered when TOT is bound in the Y537S and D538G mutants compared to the WT. Further, when compared to the WT-TOT structure, the D538G-TOT structure shows an altered conformation of the H11-12 loop and H12 occupancy of the AF-2 cleft, and multiple conformations of the TOT ligand (indicative of reduced influence on the H11-12 loop). Additionally, MD simulation of the Y537S-TOT complex shows that S537 might form a hydrogen bond with E380 that alters the antagonist conformation. Therefore, the

reduced inhibitory potency of TOT stems from its reduced affinity for the Y537S and D538G mutants along with conformational changes to the antagonist state once it occupies the ligand-binding site.

Taken together, these results suggest that the constitutive activity conferred by the Y537S and D538G mutations stems from the intrinsic ability of the mutant receptors to adopt a stable agonist conformation in the absence of hormone, thereby leading to enhanced recruitment of SRC3 coactivators and increased ERα transcriptional activity. This pre-organized agonist state contributes to a decreased affinity for hormone and especially for SERMs because the stabilized H12 agonist conformation restricts ligand access to the hormone-binding pocket. In addition to reduced ligand affinity, SERM action is further reduced by an altered antagonist state of H12. Thus, recruitment of coactivators in the breast cancer cell is not inhibited as efficiently for the Y537S and D538G mutants as for WT ERα.

One caveat to the approach described in this study is that ERα is a multi-domain protein and only the LBD was used for structural studies. To gain deeper insight into how these mutations affect full length ERα, further studies on intact multi-domain protein will be necessary. In addition, the effect of these mutations on the other aspects of ERα action including other hormone/SERM/SERD binding affinities, homo dimer formation, DNA-binding, and stability (*in vitro* and *in vivo*) and whether these mutant receptors display a differential preference for a spectrum of coactivators must be investigated.

Our findings suggest that SERMs and SERDs that are designed to specifically increase the dynamics of H12 might lead to drugs with increased potency. In this regard, our data show that the H11-12 loop plays an important and previously unrecognized role in regulating the behavior of H12, an essential molecular switch that is allosterically controlled by ligand, which determines the differential ability of the ERα AF-2 to recruit coactivators and corepressors. Therefore, antagonists with improved inhibitory potency will increase the dynamic character of mutant H12, an already appreciated aspect of SERD action (Pike et al., 2001). Additionally, our work provides a biophysical hypothesis for why fulvestrant (a SERD, known to disorder H12) was the only molecule which could completely ablate the transcriptional

activity of the Y537S and D538G mutants in breast cancer cells while TOT (a SERM) could not (Toy et al., 2013). Therefore, newly developed mixed SERM/SERDs and SERDs with improved pharmacokinetics and oral bioavailability over fulvestrant, such as AZ9496, bazedoxifene, GDC910, and RAD1901, should be particularly effective against cancers expressing the Y537S and D538G *ESR1* mutants (De Savi et al., 2015; Garner et al., 2015; Lai et al., 2015; Wardell et al., 2013). These compounds may prove invaluable for treating endocrine therapy-resistant ER+ breast cancers and also preventing or delaying the appearance of these somatic mutations in early-stage patients.

Materials and Methods

Time Resolved-FRET Assays

Protein Preparation for TR-FRET: Site-directed mutagenesis was used to generate the Y537S and D538G mutations in the ligand binding domain (LBD) of the human estrogen receptor α (ERα amino acids 304-554). The WT and mutant ERα and the nuclear receptor domain (NRD) of human SRC3 encompassing three NR boxes (amino acids 627-829) were expressed in *E. coli*, using methods reported previously (Jeyakumar et al., 2011; Carlson et al., 1997). ER LBDs of wild type, Y537S and D538G were prepared as 6×His fusion proteins, with a single reactive cysteine at C417. While bound to the Ni-NTA-agarose resin (Qiagen Inc., Santa Clarita, CA), the ERs were labeled with MAL-dPEG4-biotin (Quanta BioDesign, Powell, OH), site-specifically at C417. The SRC3-NRD construct has 4 cysteines and was labeled non-specifically, also while on the resin, with 5-iodoacetamido fluorescein (Molecular Probes, Invitrogen, Eugene, OR). It was previously determined that an average of 1.8-2 fluorescein molecules are attached to the SRC3 NRD (Kim et al., 2005).

SRC titration: SRC3 was titrated into a fixed amount of ERα-LBD-biotin mixed with SaTb (streptavidin-terbium, Invitrogen, Grand Island, NY), on 96-well black microplates (Molecular Devices, Sunnyvale, CA) following previously determined methods (Jeyakumar et al., 2011). The time-resolved

411 Förster resonance energy transfer (tr-FRET) measurements were performed with a Victor X5 plate reader
412 (Perkin Elmer, Shelton, CT) with an excitation filter at 340/10 nm and emission filters for terbium and
413 fluorescein at 495/20 and 520/25 nm, respectively, with a 100 μs delay. Diffusion-enhanced FRET was
414 determined by a parallel incubation without biotinylated ER-LBD and subtracted as a background signal.
415 The final concentrations of reagents were: 1 nM ERα-417, 0.25 nM streptavidin-terbium, 1 μM ligand,
416 SRC3-F1 coactivator titrated from 3.2×10^{-7} to 3.2×10^{-12} M. The data, representing 2-3 replicate
417 experiments, each with duplicate points, were analyzed using GraphPad Prism 4 and are expressed as the
418 EC_{50} in nM.

419 *Ligand titration:* Ligands were titrated into a constant amount of ER-LBD-biotin, SaTb, SRC3-F1.
420 The final concentrations were 1 nM ER-LBD, 0.25 nM SaTb, 100 nM SRC3-fluorescein, and increasing
421 ligand concentrations from 1×10^{-12} to 1×10^{-6} M. Diffusion-enhanced FRET was determined by a parallel
422 incubation without biotinylated ER-LBD and subtracted as a background signal. The tr-FRET was
423 measured with a Victor X5 plate reader as outlined above. The data, representing 2-3 replicate
424 experiments, each with duplicate points, was analyzed using GraphPad Prism 4, and are expressed as the
425 EC_{50} in nM.

426 **Ligand Binding Assays**

427 Relative binding affinities (RBA) were determined by a competitive radiometric binding assay with 2
428 nM [^{3}H]-E2 as tracer, as a modification of methods previously described (Katzenellenbogen et al, 1973:
429 Carlson et al., 1997). Incubations were at 0°C for 18-24 h. Hydroxyapatite was used to absorb the
430 receptor-ligand complex, and unbound ligand was washed away. The determination of RBA values is
431 reproducible in separate experiments with a CV of 0.3. The IC_{50} values for inhibition of [^{3}H]-E2 were
432 converted to K_i values using the Cheng-Prusoff equation ($K_i = IC_{50}/(1 + \text{conc. tracer}/K_d \text{ tracer})$)(Cheng
433 and Prusoff 1973); this was necessary because the affinity of the [^{3}H]-E2 tracer is different for WT and
434 mutant ERs. The K_d of [^{3}H]-E2 for the ERs was determined in a saturation binding assay, as 0.26 ± 0.13
435 nM for the WT, 1.43 ± 0.55 nM for Y537S, and 1.30 ± 0.63 nM for D538G (**Figure 2**). For the saturation

ligand binding (Scatchard analysis), protein was diluted to 0.8 nM, in Tris-glycerol buffer (50 mM Tris pH 8.0, 10% glycerol, with 0.01 M 2-mercaptoethanol and 0.3 mg/mL ovalbumin added) and incubated with various concentrations of [^{3}H]-E2 (Perkin-Elmer, Waltham, MA) in the absence or presence of a 100-fold excess of unlabeled ligand for 3-4 hours, at 0°C. Aliquots of the incubation solution were used to determine the total [^{3}H]-E2 in the sample. The incubation solutions were then assayed by adsorption onto HAP (hydroxyapatite, BioRad, Hercules, CA) and the free estradiol was washed away. Data were processed by GraphPad Prism 4 according to the method of Scatchard (Scatchard, 1949; Hurth et al., 2004).

Trypsin Proteolysis

Protein was prepared and labeled as described above for the trFRET assays. It was incubated in t/g buffer with or without 1 μM of ligand, at room temperature for 1 h. 1 μg trypsin per unit of protein was added for 10, 30, 60, and 300 minutes at room temperature according to previously established methods (Tamrazi et al., 2003). FRET signal was measured using a Victor X5 plate reader as outlined above. The data, representing 2-3 replicate experiments, were analyzed using GraphPad Prism 4, and are expressed as half-lives ($t_{1/2}$).

Hydrogen Deuterium Exchange

Differential hydrogen/deuterium exchange (HDX) MS. Solution-phase amide HDX experiments were carried out using a fully automated system as described previously with slight modifications.(Chalmers et al., 2006) Prior to HDX, 10 μM of 6×-HIS-ERα-LBD (WT or mutants) were incubated with 100 μM of individual ligands for 1 h on ice for complex formation. Differential HDX experiments with ligands were initiated by mixing either 5 μl of the ERα LBD alone (*apo*) or the complex (1:10 molar mixture of ERα and ligands) with 20 μl of D_2O-containing HDX buffer (20 mM Tris 8.0, 150 mM NaCl, and 3 mM DTT). For the differential HDX experiments with SRC3 NRD, 10 μM of WT or mutant ERα LBDs were mixed with 25μM of SRC3 NRD for 2 h on ice for complex formation and then subjected to HDX as described above. For the *apo* ERα comparisons, 10 μM of WT or mutant ERα LBDs were run in a similar

differential format comparing either Y537S or D538G directly with the WT. 25 µl aliquots were drawn after 0 s, 10 s, 30 s, 60 s, 900 s or 3,600 s of on-exchange at 4°C and the protein was denatured by the addition of 25 µl of a quench solution (1% v/v TFA in 5 M urea and 50 mM TCEP). Samples were then passed through an immobilized pepsin column at 50 µl min^{-1} (0.1% v/v TFA, 15°C) and the resulting peptides were trapped on a C_8 trap column (Hypersil Gold, ThermoFisher, Grand Island, NY). The bound peptides were then gradient-eluted (5-50% CH_3CN w/v and 0.3% w/v formic acid) across a 1 mm × 50 mm C_{18} HPLC column (Hypersil Gold, ThermoFisher, Grand Island, NY) for 8 min at 4°C. The eluted peptides were then subjected to electrospray ionization directly coupled to a high resolution Orbitrap mass spectrometer (LTQ Orbitrap XL with ETD, Thermo Fisher).

Peptide Identification and HDX data processing: MS/MS experiments were performed with a LTQ linear ion trap mass spectrometer (LTQ Orbitrap XL with ETD, Thermo Fisher) over a 70-min gradient. Product ion spectra were acquired in a data-dependent mode and the five most abundant ions were selected for the product ion analysis. The MS/MS *.raw data files were converted to *.mgf files and then submitted to Mascot (Matrix Science, London, UK) for peptide identification. Peptides included in the peptide set used for HDX detection had a MASCOT score of 20 or greater. The MS/MS MASCOT search was also performed against a decoy (reverse) sequence, and false positives were ruled out. The MS/MS spectra of all the peptide ions from the MASCOT search were further manually inspected, and only the unique charged ions with the highest MASCOT score were used in estimating the sequence coverage. The intensity-weighted average m/z value (centroid) of each peptide isotopic envelope was calculated with the latest version of our in-house software, HDX Workbench (Pascal et al., 2012). HDX data are presented as an average of three independent triplicates. Deuterium uptake for each peptide is calculated as the average of % D_2O for the 6 time points (10s, 30s, 60s, 300s, 900s and 3600s) and the difference in average % D_2O values between the *apo* and liganded states is presented as a heat map with a color code given at the bottom of each figure (warm colors for deprotection and cool colors for protection) and colored only if they show a >5% difference (less or more protection) between the two states and if atleast

two time points show a statistically significant difference in a paired two-tailed student's t-test ($p<0.05$). Grey color represents no significant change (0-5%) between the two states. The exchange at the first two residues for any given peptide is rapid and is ignored in the calculations. Each peptide bar in the heat map view displays the average Δ $\%D_2O$ values with its associated standard deviation and the charge state shown in parentheses.

X-ray Crystallographic Analysis of the D538G ERα LBD

Generation and Production of the D538G ERα LBD Mutant: Quick Change Mutagenesis (New England Biolabs, Ipswitch, MA) was performed to change aspartate 538 to glycine on a pGM6 containing the gene for the 6×His-Tobacco etch virus (TEV)-ERα LBD. The following oligonucleotide primers were used to generate the mutant:

Forward: (*5'*GGTGCCCCTCTACGGCCTGCTGCTGG*3'*)

Reverse: (*5'*CCAGCAGCAGGCCGTAGAGGGGCACC*3'*)

The sequence for the resulting ERα LBD D538G mutant was verified by DNA sequencing.

Protein Expression for Crystal Generation: A 250 mL LB broth containing 100 µg/mL ampicillin was inoculated with a single colony of the *E. coli* expression strain BL21 (DE3) transformed with pGM6-ERα LBD D538G mutant. Following overnight incubation at 37°C, 10×1L LB broth containing 100 µg/mL ampicillin were each inoculated with 5 mL aliquots of the overnight culture. Cells grew at 37°C with shaking at 180 rpm until they reached mid-log phase growth (OD_{600} = 0.8) at which point expression of the protein was induced with 0.3 mM IPTG and incubation continued overnight with shaking at 20°C. Cells were harvested by centrifugation at 3,500 *g* for 30 minutes, and the pellet was frozen at -20°C. The pellet was resuspended in 200 mL BPER and 100 µg DNAse, protein inhibitor cocktail, and lysozyme were added to the lysate. Following 30 minutes of stirring at 4°C, the lysed cells were centrifuged at 22,000 *g* for 30 minutes and the supernatant isolated. The soluble fraction was incubated with 2 mL of

pre-washed Ni-NTA resin (ThermoFisher, Grand Island, NY) then placed onto a column. The column was washed with 10 column volumes of buffer containing 20 mM Tris pH 8.0, 500 mM NaCl, 40 mM imidazole pH 8.0, 10% glycerol, and 15 mM 2-mercaptoethanol, and the protein was subsequently eluted from the column using a buffer containing 20 mM Tris pH 8.0, 500 mM NaCl, 500 mM imidazole pH 8.0, 10% glycerol, and 15 mM 2-mercaptoethanol. The 6×His-TEV tag was removed using a 15:1 w/w ratio of LBD to TEV protease. The LBD was isolated from the tag by a pass over a column containing 2 mL of washed Ni-NTA resin and the flow through, containing the LBD, was isolated. The protein was dialyzed overnight in a buffer containing 20 mM Tris pH 8.0, 20 mM NaCl, 10% glycerol and 15 mM 2-mercaptoethanol then subjected to a final purification on a Resource Q ion exchange column (ThermoFisher, Grand Island, NY). A 100 mL linear gradient was used to elute the protein with a buffer containing 20 mM Tris pH 8.0, 500 mM NaCl, 10% glycerol and 15 mM 2-mercaptoethanol. A single peak corresponding to the ERα LBD D538G mutant was isolated and a single band was observed on a SDS-PAGE gel (BioRad, Hercules, CA). Lastly, the LBD was concentrated to 10 mg/mL using a spin concentrator, separated into 100 µL aliquots, flash frozen, and stored at -80 °C until use.

Crystallization of the ERα LBD D538G Mutant: For the estradiol (E2) and 4-hydroxytamoxifen (TOT)-bound structures, the purified ERα LBD D538G mutant at 10 mg/mL was incubated for overnight with 1 mM ligand. For the *apo* D538G and E2 structures a 2.5-fold mol:mol (excess) of glucocorticoid receptor interacting protein NR box II peptide (GRIP) was incubated with the LBD for approximately 3 hours. Hanging drop method was used for all crystals using VDX pre-greased plates (Hampton Research, Aliso Viejo, CA). For the *apo* D538G structure, 15 mM $MgCl_2$ and 10 mM ATP were added to the protein prior to plating. A total of 1 µL of 5 mg/mL *apo* D538G was mixed with 1 µL of 30% PEG 3,350, 200 mM $MgCl_2$ and 100 mM Tris pH 8.5. For the E2-complex structure a total of 1 µL of 5 mg/mL protein was mixed with 1 µL of 25% PEG 3,350, 200 mM $MgCl_2$, 100 mM Tris pH 8.5 and 1 mM phenylalanine. For the D538G-TOT complex structure, the protein/ligand was centrifuged at 19,000 *g* to remove precipitate then 2 µL at 10 mg/mL was mixed with 2 µL of 400 mM ammonium sulfate, 100 mM

Tris pH 8.0 and 10% glycerol. For the *apo* and E2-bound structures, clear triangular rods appeared after 3 days. For the TOT-bound structure, clear rectangular rods appeared overnight. Paratone-N was used as the cryo-protectant for the *apo* and TOT-bound structures, whereas 25% glycerol was used as the cryo-protectant for the E2-bound structure. All x-ray data sets were collected at the Advanced Photon Source at Argonne National Laboratories, Argonne, Illinois. The TOT-complex data set was collected at the SBC 19-BM beamline (0.97 Å), the E2-bound structure at LS-CAT 21-ID-D (0.97 Å), and the *apo* structure at LS-CAT 21-ID-F (0.97 Å).

X-ray Structure Solution: Data were indexed, scaled and merged using HKL-3000(Otwinowski and Minor, 1997). Phaser was used for all molecular replacements (McCoy et al., 2007). An existing structure of the WT ERα LBD in complex with TOT (PDB: 3ERT) was modified by removing all ligands and water molecules, and then used as the search molecule for the D538G-TOT structure (Shiau et al., 1998). For the WT and *apo* D538G structures, an existing WT ERα LBD-agonist structure (PDB: 2QXM) was modified by removing all ligands and water molecules, and then used as the search molecule (Nettles et al., 2008). For the *apo* and E2-bound structures, one dimer was found in the asymmetric unit (ASU), whereas four dimers were found for the TOT-bound structure. The CCP4i (Refmac) program suite was used for all refinement (Winn et al., 2011). The models were refined using iterative rounds of Refmac and Coot. Densities for the ligands were clearly visible after the first round of refinement for both the E2- and TOT-bound structures. Unresolved residues were not included in the structures deposited in the Protein Data Bank including the *apo* D538G (PDB: 4Q13), D538G-E2 complex (PDB: 4PXM), and D538G-4OHT (PDB: 4Q50) structures. All x-ray crystal structure images were made using Pymol.

Molecular Dynamics (MD) Simulations of D538G

Structure Preparation: Atomistic molecular models of dimeric ERα were constructed *in silico* starting from an x-ray crystal structure of ERα in complex with E2 and a coactivator peptide (Wärnmark et al., 2002). Atomic coordinates were downloaded from the Protein Data Bank (PDB code: 1GWR) and

559 prepared using a combination of the MOE (Molecular Operating Environment, 2014) and VMD (Visual
560 Molecular Dynamics; Humphrey et al., 1996). Using the Structure Preparation module within MOE, all
561 missing loops were constructed, explicit hydrogen atoms added, a side chain rotamer search was
562 performed, and protonation states were computed for all titratable residues. The resulting structure was
563 loaded into VMD, where each protein monomer, coactivator peptide, and all crystallographic water
564 molecules were written to separate PDB files; the E2 ligand coordinates were discarded for simulated *apo*
565 structures. Each histidine residue was renamed according to the CHARMM naming convention to reflect
566 the computed protonation states, as shown in **Table 4**. The dimeric ERα structure was then constructed
567 from the separate PDB files using the PSFGEN plugin within VMD. The N- and C-termini were capped
568 with neutral acetyl and *N*-methylamido groups, respectively. The protein complex was subsequently
569 solvated using the SOLVATE plugin of VMD with a 20-Å padding thickness on all sides, and ions were
570 added using the AUTOIONIZE plugin to neutralize the system and yield a final NaCl concentration of 0.1
571 M. Ions were placed a minimum distance of 5 Å from the protein surface. The resulting fully solvated
572 system contained ~101k atoms. The D538G mutant structure was constructed in an analogous manner,
573 differing only in an additional "mutate" command in PSFGEN to create the D538G mutation. Additional
574 steps to minimize and equilibrate the mutated region are discussed below.

575 *Simulations:* All MD simulations were performed using the NAMD2 software package (Phillips et
576 al., 2005). The CHARMM36 force field was used to describe the protein, solvent, and ions, and included
577 CMAP backbone corrections and NBFIX terms for protein-ion interactions (Mackerell et al., 1998;
578 Mackerell, 2004). The TIP3P water model was used to as the explicit solvent (Jorgensen et al., 1983).
579 Ligand parameters for E2 were taken from the CHARMM General Force Field (CGenFF;
580 Vanommesleaghe et al., 2010) as assigned by analogy using the ParamChem (Vanommeslaeghe and
581 MacKerell, 2012a) webserver. Attempts to further refine torsion parameters with moderate penalty scores
582 using the Force Field Toolkit (ffTk; Mayne et al., 2013) did not yield significant improvement of the
583 potential energy surface. Simulations were performed under an NPT ensemble at 1.0 atm and 310 K,

584 employing a Nosé-Hoover thermostat and a Langevin piston with a period of 100 fs, decay of 50 fs, and
585 damping coefficient of 0.5 ps^{-1} (Martyna et al., 1994; Feller et al., 1995). A simulation time step of 2 fs
586 was used, and atomic coordinates were recorded every 500 steps (1 ps). The molecular system employed
587 periodic boundary conditions, and non-bonded interactions were truncated using a switching function
588 from 10.0 to 12.0 Å. Long range electrostatics were evaluated using the particle mesh Ewald (PME)
589 method (Darden et al., 1993). Bonded and non-bonded forces were computed at every time step, while
590 PME forces were computed every other time step.

591 All molecular systems were first simulated to equilibrate "non-natural" components of the system by
592 applying harmonic restraints (k = 1 kcal/mol/$Å^2$) on heavy atoms present in the 1GWR x-ray crystal
593 structure. Atoms belonging to added water, ions, missing loops (±2 residues), or mutated residues (±2
594 residues) were left unrestrained. The system was subjected to a 10,000-step downhill minimization,
595 followed by 1 ns of simulation. All restraints were then released and the system was simulated for an
596 additional 100 ns of production simulation.

597 *MD Simulation Trajectory Analysis:* All analyses were performed using VMD (Humphrey et al.,
598 1996). Simulation trajectories were first prepared by removing water molecules, concatenating sequential
599 trajectory files, downsampling the framerate to 10 ps/frame, and rewrapping the periodic system to move
600 the protein center of mass to the center of the periodic cell. Prior to analysis, all trajectories were aligned
601 to the initial frame by fitting Cα atoms of the protein, excluding the coactivator peptides from the fit
602 measurement. When a consistent reference frame was required for cross-trajectory comparisons, all
603 frames were aligned to the 1GWR x-ray structure prior to analysis. With the exception of explicit time
604 series measurements (*i.e.*, SASA), all other analyses were performed for the last 50 ns of the 100-ns
605 production simulation.

606 Side chain conformations of residue Y537 were visualized by superimposing the position of the
607 phenolic oxygen every 100 ps (n = 500) using the standard "points" representation of VMD. Density

maps of side chain and backbone atoms were computed using the VOLMAP plugin of VMD with a resolution of 1 Å and averaging the mass-weighted density over the trajectory. The volumetric maps for visualizing the side chain positions were set to the 0.75 isosurface, representing the volume containing atomic density for greater than 75% of the analyzed trajectory. Ramachandran analysis was performed by measuring the φ and ψ dihedral angles for each residue at a 10-ps interval (n = 5,000). The data were then converted to a two-dimensional histogram and plotted using the Matplotlib package of the python programming language (Hunter, 2007). A Gaussian filter was used to smooth the data ($\sigma = 10.0$), and the resulting bins were grouped into 10 contours. The lowest intensity contour (background, dark blue) was removed for clarity. The solvent accessible surface area (SASA) was computed for the side chains of hydrophobic residues 533-536 using the built-in "measure sasa" function of VMD. The default probe radius of 1.4 Å was used while taking the surrounding protein environment into account. SASA measurements were computed at 10-ps intervals (n = 10,000) over the entire production simulation and smoothed using a Gaussian-weighed running average ($\sigma = 10.0$).

Molecular Dynamics Simulations of Y537S-TOT Complex

A parameter set was constructed for TOT. Its structure was optimized quantum mechanically at the level of restricted Hartree-Fock (RHF) 6-31g* using the computer program Gaussian 03 (Gaussian 03, Revision C.02, Frisch et al., 2004). The partial atomic charges of TOT were then derived with Restrained ElectroStatic Potential (RESP) (Bayly et al., 1993; Cornell et al., 1993) fitting to the quantum mechanical RHF/6-31g* potential. The ideal geometry was defined as the optimized. The other molecular mechanical parameters were derived by assigning CHARMm22 atom types for TOT (Momany and Rone, 1992).

The dimer with the least missing residues of the H11-H12 loop was selected from the D538G-TOT crystal structure and served as the template structure to model the Y537S-TOT dimer structure. The side chain atoms at positions 537 and 538 were removed, and then desired side chain atoms were placed with the other missing atoms using the default geometry parameters in CHARMm22. Hydrogen atoms were

placed with the hbuild module of the computer program CHARMM (Brünger and Karplus, 1988; Vanommeslaeghe and MacKerell, 2012b). Missing residues (loops) in the starting crystal structure were optimized in three rounds (100 steps of the steepest descent method followed by two rounds of 100 steps of the adopted New-Raphson method) with updated harmonic constraints on the other atoms. Then all newly-added atoms' positions were optimized in the same fashion.

The resulting minimized structure was solvated with water molecules of 15 Å padding thickness from the molecular boundary and ionized to reach charge neutrality and the concentration of 0.145 M, both of which were done with VMD (Humphrey et al., 1996). The system was minimized for 5000 steps before a 100-ns MD simulation using NAMD2 (Phillips et al., 2005) was performed.

Acknowledgements

The authors would like to acknowledge funding from the Department of Defense Breast Cancer Research Program Breakthrough Award BC131458P1, the Susan G. Komen Foundation PDF14301382 (to S.W.F.), NIH P41-GM104601 (to E.T.), NIH T32ES007326 (to T.A.M.), NIH R01-DK015556 (to J.A.K), NIH U54-MH084512 (to P.R.G. PI: Rosen), Landenberger Foundation (to V.D.), and NSF CCF-1546278 (to Y.S.). Supercomputing resources were provided through NSF XSEDE allocations (MCB104105 and MCB140135 to J.A.K.). All x-ray crystal structure data sets were collected at Argonne National Laboratory, Structural Biology Center and the Life Sciences Collaborative Access team at the Advanced Photon Source. Argonne is operated by UChicago Argonne, LLC, for the U.S. Department of Energy, Office of Biological and Environmental Research under contract DE-AC02-06CH11357. Special thanks to Dr. David Hosfield for critical reading and suggested edits.

References Cited

Bayly,Christopher I., Piotr Cieplak, Wendy D. Cornell, and Peter A Kollman. 1993. “A Well-Behaved Electrostatic Potential Based Method Using Charge Restraints for Deriving Atomic Charges: The RESP Model.” *The Journal of Physical* 97: 10269–80. doi:10.1021/j100142a004.

Brünger, Axel T. and Martin Karplus. 1988. “Polar Hydrogen Positions in Proteins: Empirical Energy Placement and Neutron Diffraction Comparison.” *Proteins* 4 (2): 148–56. doi:10.1002/prot.340040208.

Carlson, Kathryn E., Inho Choi, Arvin Gee, Benita S. Katzenellenbogen, and John A. Katzenellenbogen. 1997. “Altered Ligand Binding Properties and Enhanced Stability of a Constitutively Active Estrogen Receptor: Evidence That an Open Pocket Conformation Is Required for Ligand Interaction.” *Biochemistry* 36 (48): 14897–905. doi:10.1021/bi971746l.

Chalmers, Michael J., Scott A. Busby, Bruce D. Pascal, Yuanjun He, Christopher L. Hendrickson, Alan G. Marshall, and Patrick R. Griffin. 2006. “Probing Protein Ligand Interactions by Automated Hydrogen / Deuterium Exchange Mass Spectrometry” *Anal. Chem.* 78 (4): 1005–14. doi:10.1021/ac051294f

Cheng, Yung-Chi and William H. Prusoff. 1973. "Relationship Between the Inhibition Constant (K_I) and the Concentration of Inhibitor Which Causes 50 Per Cent Inhibition (I_{50}) of an enzymatic reaction." *Biochemical Pharmacology* 22, 3099-108. doi:10.1016-0006-2952(73)90196-2.

Cornell, Wendy D., Piotr Cieplak, Christopher I. Bayly, and Peter a. Kollman. 1993. “Application of RESP Charges To Calculate Conformational Energies, Hydrogen Bond Energies, and Free Energies of Solvation.” *Journal of the American Chemical Society* 115 (7): 9620–31. doi:10.1021/Ja00074a030.

Darden, Tom, Darrin York, and Lee Pedersen. 1993. “Particle Mesh Ewald: An N·log(N) Method for Ewald Sums in Large Systems.” *The Journal of Chemical Physics* 98 (12): 10089. doi:10.1063/1.464397.

De Savi, Chris, Robert H. Bradbury, Alfred A. Rabow, Richard A. Norman, Camila de Almeida, David M. Andrews, Peter Ballard, et al. 2015. "Optimization of a Novel Binding Motif to (E)‐3-(3,5-Difluoro-4-((1R,3R)‐2-(2-fluoro-2-methylpropyl)-3-methyl-2,3,4,9-tetrahydro‐1H‐pyrido[3,4‐b]indol-1-yl)phenyl)acrylic Acid (AZD9496), a Potent and Orally Bioavailable Selective Estrogen Receptor Downregulator and Antagonist." *J.Med.Chem.* 58, 8128-8140. doi:10.1021/acs.jmedchem.5b00984.

Eiler, Sylvia, Monique Gangloff, Sylvie Duclaud, Dino Moras, and Marc Ruff. 2001. “Overexpression, Purification, and Crystal Structure of Native ER Alpha LBD.” *Protein Expression and Purification* 22 (2): 165–73. doi:10.1006/prep.2001.1409.

Feller, Scott E., Yuhong Zhang, Richard W. Pastor, and Bernard R. Brooks. 1995. “Constant Pressure Molecular Dynamics Simulation: The Langevin Piston Method.” *The Journal of Chemical Physics* 103 (11): 4613. doi:10.1063/1.470648.

Gangloff, Monique, Marc Ruff, Sylvia Eiler, Sylvie Duclaud, Jean M Wurtz, and Dino Moras. 2001. “Crystal Structure of a Mutant hER alpha Ligand-Binding Domain Reveals Key Structural Features for the Mechanism of Partial Agonism.” *The Journal of Biological Chemistry* 276 (18): 15059–65. doi:10.1074/jbc.M009870200.

Garner, Fiona, Maysoun Shomali, Dotty Paqui, C. Richard Lyttle, and Gary Hattersley. 2015. "RAD1901: a Novel, Orally Bioavailable Selective Estrogen Receptor Degrader that Demonstrates Antitumor Activity in Breast Cancer Xenograft Models." *Anti-Cancer Drugs* 26: 948-58. doi:10.1097/CAD.0000000000000271

Frisch, M. J., Frisch, G. W. Trucks, H. B. Schlegel, G. E. Scuseria, M. A. Robb, J. R. Cheeseman, J. A. Montgomery, Jr., T. Vreven, K. N. Kudin, J. C. Burant, J. M. Millam, S. S. Iyengar, J. Tomasi, V. Barone, B. Mennucci, M. Cossi, G. , and J. A. Pople. 2004. “Gaussian 03, Revision C.02.”

Horn, James R., Brian Kraybill, Elizabeth J. Petro, Stephen J. Coales, Jeffrey A. Morrow, Yoshitomo Hamuro, and Anthony A. Kossiakoff. 2006. “The Role of Protein Dynamics in Increasing Binding Affinity for an Engineered Protein-Protein Interaction Established by H/D Exchange Mass Spectrometry.” *Biochemistry* 45: 8488–98. doi:10.1021/bi0604328.

Humphrey, William, Andrew Dalke, and Klaus Schulten. 1996. “VMD : Visual Molecular Dynamics” 7855 (October 1995): 33–38.

Hunter, J.D. 2007. “Matplotlib: A 2D Graphic Environment.” American Institute of Physics. http://ieeexplore.ieee.org/xpl/articleDetails.jsp?arnumber=4160265.

Hurth, Kyle M., Mark J Nilges, Kathryn E Carlson, Anobel Tamrazi, R Linn Belford, and John A Katzenellenbogen. 2004. “Ligand-Induced Changes in Estrogen Receptor Conformation As Measured by Site-Directed Spin Labeling,” *Biochemistry* 43(7): 1891–1907. doi:10.1021/bi0355660p.

Jeselsohn, Rinath, Roman Yelensky, Gilles Buchwalter, Garrett Frampton, Funda Meric-Bernstam, Ana Maria Gonzalez-Angulo, Jaime Ferrer-Lozano, et al. 2014. “Emergence of Constitutively Active Estrogen Receptor-α Mutations in Pretreated Advanced Estrogen Receptor-Positive Breast Cancer.” *Clinical Cancer Research* 20 (7): 1757–67. doi:10.1158/1078-0432.CCR-13-2332.

Jeyakumar, Muthu, Kathryn E. Carlson, Jillian R. Gunther, and John A. Katzenellenbogen. 2011. “Exploration of Dimensions of Estrogen Potency: Parsing Ligand Binding and Coactivator Binding Affinities.” *The Journal of Biological Chemistry* 286 (15): 12971–82. doi:10.1074/jbc.M110.205112.

Jorgensen, William L., Jayaraman Chandrasekhar, Jeffry D. Madura, Roger W. Impey, and Michael L. Klein. 1983. “Comparison of Simple Potential Functions for Simulating Liquid Water.” *The Journal of Chemical Physics* 79 (2): 926. doi:10.1063/1.445869.

Katzenellenbogen, John A., Howard J. Johnson, and Harvey N Myers. 1973. “Photoaffinity Labels for Estrogen Binding” *Biochemistry* 12 (21): 4085–92.doi:10.1021/bi00745a010

Kim, Sung Hoon, Anobel Tamrazi, Kathryn E. Carlson, and John A. Katzenellenbogen. 2005. “A Proteomic Microarray Approach for Exploring Ligand-Initiated Nuclear Hormone Receptor Pharmacology, Receptor Selectivity, and Heterodimer Functionality.” *Molecular & Cellular Proteomics* 4 (3): 267–77. doi:10.1074/mcp.M400192-MCP200.

Lai, Andiliy, Mehmet Kahraman, Steven Govek, Johnny Nagasawa, Celine Bonnefous, Jackie Julien, Karensa Douglas. 2015. "Identification of GDC-0810 (ARN-810), an Orally Bioavailable Selective Estrogen Receptor Degrader (SERD) that Demonstrates Robust Activity in Tamoxifen-Resistant Breast Cancer Xenografts." *J.Med.Chem.* 58, 4888-904. doi:10.1021/acs.jmedchem.5b0054.

Li, Shunqiang., Dong Shen, Jieya Shao, Robert Crowder, R., Wenbin Liu, Aleix Prat, Xiaping He, Shuying Liu, Jeremy Hoog, Charles Lu, Li Ding, Obi L. Griffith, Christopher Miller, Dave Larson, Robert S. Fulton, Michelle Harrison, Tom Mooney, Joshua F. McMichael, Jingqin Luo, Yu Tao, Rodrigo Goncalves, Christopher Schlosber. 2014. “Endocrine-Therapy Resistant ESR1 Variants Revealed by Genomic Characterization Fo Breast-Cancer-Derived Xenografts.” *Cell Reports* 4 (6): 1–28. doi:10.1016/j.celrep.2013.08.022.

Liao, Lan, Shao-Qing Kuang, Yuhui Yuan, Sonia M. Gonzalez, Bert W. O’Malley, and Jianming Xu. 2002. “Molecular Structure and Biological Function of the Cancer-Amplified Nuclear Receptor Coactivator SRC-3/AIB1.” *The Journal of Steroid Biochemistry and Molecular Biology* 83: 3–14. doi:10.1016/S0960-0760(02)00254-6.

Mackerell, A D, D Bashford, M Bellott, R L Dunbrack, J D Evanseck, M J Field, S Fischer, et al. 1998. “All-Atom Empirical Potential for Molecular Modeling and Dynamics Studies of Proteins” *Journal of Phyical Chemistry* 5647 (97): 3586–3616. doi:10.1021/jp973084f.

Mackerell, Alexander D. 2004. “Empirical Force Fields for Biological Macromolecules: Overview and Issues.” *Journal of Computational Chemistry* 25 (13): 1584–1604. doi:10.1002/jcc.20082.

Martyna, Glenn J., Douglas J. Tobias, and Michael L. Klein. 1994. “Constant Pressure Molecular Dynamics Algorithms.” *The Journal of Chemical Physics* 101 (5): 4177. doi:10.1063/1.467468.

Mayne, Christopher G., Jan Saam, Klaus Schulten, Emad Tajkhorshid, and James C. Gumbart. 2013. “Rapid Parameterization of Small Molecules Using the Force Field Toolkit.” *Journal of Computational Chemistry* 34: 2757–70. doi:10.1002/jcc.23422.

McCoy, Airlie J., Ralf W. Grosse-Kunstleve, Paul D. Adams, Martyn D. Winn, Laurent C. Storoni, and Randy J. Read. 2007. “Phaser Crystallographic Software.” *Jounal of Applied Crystallography* 40: 658–74.doi:10.1107/S0021889807021206.

Merenbakh-Lamin, Keren, Noa Ben-Baruch, Adva Yeheskel, Addie Dvir, Lior Soussan-Gutman, Rinath Jeselsohn, Roman Yelensky, et al. 2013. “D538G Mutation in Estrogen Receptor-A: A Novel Mechanism for Acquired Endocrine Resistance in Breast Cancer.” *Cancer Research* 73 (23): 6856–64. doi:10.1158/0008-5472.CAN-13-1197.

“Molecular Operating Environment (MOE).” 2014. Montreal, QC, Canada: Chemical Computing Group Inc. http://www.chemcomp.com/.

768 Momany, Frank A. and Rebecca Rone. 1992. “Validation of the General Purpose QUANTA
769 3.2/CHARMm Force Field.” *Journal of Computational Chemistry* 13 (7): 888–900.
770 doi:10.1002/jcc.540130714.

771 Nettles, Kendall W., John B. Bruning, German Gil, Jason Nowak, Sanjay K. Sharma, Johnnie B. Hahm,
772 Kristen Kulp, et al. 2008. “NFkappaB Selectivity of Estrogen Receptor Ligands Revealed by
773 Comparative Crystallographic Analyses.” *Nature Chemical Biology* 4 (4): 241–47.
774 doi:10.1038/nchembio.76.

775 Otwinowski, Zbyszek and Wladek Minor. 1997. “Processing of X-Ray Diffraction Data Collected in
776 Oscillation Mode.” *Methods Enzymol* 276: 307–26.

777 Pascal, Bruce D., Scooter Willis, Janelle L. Lauer, Rachelle R. Landgraf, Graham M. West, David
778 Marciano, Scott Novick, Devrishi Goswami, Michael J. Chalmers, and Patrick R. Griffin. 2012.
779 “HDX Workbench: Software for the Analysis of H/D Exchange MS Data.” *Journal of the American*
780 *Society for Mass Spectrometry* 23 (9): 1512–21. doi:10.1007/s13361-012-0419-6.

781 Phillips, Chris, Lee R. Roberts, Markus Schade, Richard Bazin, Andrew Bent, Nichola L. Davies, Rob
782 Moore, et al. 2011. “Design and Structure of Stapled Peptides Binding.” *JACS* 133(25): 9696–99.

783 Phillips, James C., Rosemary Braun, Wei Wang, James Gumbart, Emad Tajkhorshid, Elizabeth Villa,
784 Christophe Chipot, Robert D. Skeel, Laxmikant Kalé, and Klaus Schulten. 2005. “Scalable
785 Molecular Dynamics with NAMD.” *Journal of Computational Chemistry* 26 (16): 1781–1802.
786 doi:10.1002/jcc.20289.

787 Pike, Ashley C. W., A. Marek Brzozowski, Julia Walton, Roderick E Hubbard, Ann-Gerd Thorsell, Yi-
788 Lin Li, Jan-Åke Gustafsson and Mats Carlquist. 2001. “Structural Insights into the Mode of Action
789 of a Pure Antiestrogen” *Structure* 9 (01): 145–53. doi:10.1016/S0969-2126(01)00568-8.

790 Ramachandran, Gopalasamadrum N., C. Ramakrishnan, and V. Sasisekharan. 1963. “Stereochemistry of
791 Polypeptide Chain Configurations.” *Journal of Molecular Biology* 7 (1). Academic Press Inc.
792 (London) Ltd.: 95–99. doi:10.1016/S0022-2836(63)80023-6.

793 Robinson, Dan R., Yi-Mi Wu, Pankaj Vats, Fengyun Su, Robert J. Lonigro, Xuhong Cao, Shanker
794 Kalyana-Sundaram, et al. 2013. “Activating ESR1 Mutations in Hormone-Resistant Metastatic
795 Breast Cancer.” *Nature Genetics* 45 (12): 1446–51. doi:10.1038/ng.2823.

796 Scatchard, George. “The Attractions of Proteins for Small Molecules and Ions.” *Annals of the New York*
797 *Academy of Sciences* 51(4): 660–72. doi:10.111/j.1749-6632.1949.tb21297.x

798 Shiau, Andrew K., Danielle Barstad, Paula M. Loria, Lin Cheng, Peter J. Kushner, David A. Agard, and
799 Geoffrey L. Greene. 1998. “The Structural Basis of Estrogen Receptor/Coactivator Recognition and
800 the Antagonism of This Interaction by Tamoxifen.” *Cell* 95 (7): 927–37.doi:10.106/S0092-
801 8674(00)81717-1.

802 Steffen, Claudia, Klaus Thomas, Uwe Huniar, Arnim Hellweg, Oliver Rubner, and Alexander Schroer.
803 2010. “TmoleX--a Graphical User Interface for TURBOMOLE.” *Journal of Computational*
804 *Chemistry* 31: 2967–70. doi:10.1002/jcc.

Strasser-Weippl, Kathrin, and Paul E. Goss. 2005. “Advances in Adjuvant Hormonal Therapy for Postmenopausal Women.” *Journal of Clinical Oncology : Official Journal of the American Society of Clinical Oncology* 23 (8): 1751–59. doi:10.1200/JCO.2005.11.038.

Tamrazi, Anobel, Kathryn E Carlson, Alice L Rodriguez, and John A Katzenellenbogen. 2005. “Coactivator Proteins as Determinants of Estrogen Receptor Structure and Function: Spectroscopic Evidence for a Novel Coactivator-Stabilized Receptor Conformation.” *Molecular Endocrinology* 19 (6): 1516–28. doi:10.1210/me.2004-0458.

Toy, Weiyi, Yang Shen, Helen Won, Bradley Green, Rita a Sakr, Marie Will, Zhiqiang Li, et al. 2013. “ESR1 Ligand-Binding Domain Mutations in Hormone-Resistant Breast Cancer.” *Nature Genetics* 45 (12): 1439–45. doi:10.1038/ng.2822.

Vanommeslaeghe, Kenno, and Alexander D. MacKerell. 2012. “Automation of the CHARMM General Force Field (CGenFF) I: Bond Perception and Atom Typing.” *Journal of Chemical Information and Modeling* 52 (1): 3144–54. doi:10.1021/ci300363c.

Wardell, Suzanne E., Erik R. Nelson, Christina A. Chao, and Donald P. McDonnell. 2013. "Bazedoxifene Exhibits Antiestrogenic Activity in Animal Models of Tamoxifen Resistant Breast Cancer; Implications for Treatment of Advanced Disease." *Clin Cancer Res.* 19(9): 2420-31. doi:10.1158/1078-0432.CCR-12-3771.

Weis, Karen E., Kirk Ekena, James A. Thomas, Gwendal Lazennec, and Benita S. Katzenellenbogen. 1996. “Constitutively Active Human Estrogen Receptors Containing Amino Acid Substitutions for Tyrosine 537 in the Receptor Protein.” *Molecular Endocrinology* 10(11): 1388–98.doi:10.11.8923465.

Winn, Martyn D., Charles C. Ballard, Kevin D. Cowtan, Eleanor J. Dodson, Paul Emsley, Phil R. Evans, Ronan M. Keegan, et al. 2011. “Overview of the CCP4 Suite and Current Developments.” *Acta Crystallographica. Section D, Biological Crystallography* 67 (Pt 4). International Union of Crystallography: 235–42. doi:10.1107/S0907444910045749.

Zhang, Qiu-xia, Åke Borg, Douglas M. Wolf, Steffi Oesterreich, and Suzanne A. W Fuqua. 1997. “An Estrogen Receptor Mutant with Strong Hormone-Independent Activity from a Metastatic Breast Cancer.” *Cancer Research* 57(7): 1244–49.

Figure Legends

Figure 1: Binding of the SRC3 coactivator to WT, Y537S, or D538G ERα LBD in the absence or presence of E2 or TOT.

Figure 1-figure supplement 1: Binding of the SRC3 coactivator to WT, Y537S, or D538G mutant ERα LBD with increasing concentrations of E2 or TOT.

Figure 2: Determination of K_d values of estradiol (E2) binding to wild type, Y537S, and D538G LBDs, by a direct binding assay. All slopes had an r^2 of 0.95 or better; shown is a representative experiment. For details, see Methods.

Figure 3: Relative binding affinity assay of wild type, Y537S, and D538G LBDs, showing the TOT competition curves. With all proteins, the E2 curve is set to 100% and is shown only once. For details, see Methods.

Figure 4: Conformational stability of WT and mutant ERα LBD H11-12 loop and H12. A) Proteolytic susceptibility of the WT, Y537S and D538G ERα LBD mutants in the *apo*, E2-bound, and TOT-bound states. B-C) Deuterium uptake plot for the c-terminus of H11 along with the H11-12 loop and H12 for the *apo* WT vs Y537S ERα LBD (B), *apo* WT vs D538G ERα LBD (C). All HDX MS data represent an average of 3 replicates and are color coded from red to blue with warm colors representing increased conformational dynamics (red being the highest D_2O uptake) and cool colors representing decreased conformational dynamics (blue being the lowest D_2O uptake). All regions colored were determined to be statistically significant based on a paired two-tailed Students t-test. A legend is provided at the bottom. Grey indicates no statistically significant change between the two *apo* states.

Figure 4-figure supplement 1: Complete differential amide HDX MS map of WT ERα LBD binding to E2.

Figure 4-figure supplement 2: Complete differential amide HDX MS map of Y537S ERα LBD mutant binding to E2.

Figure 4-figure supplement 3: Complete differential amide HDX MS map of D538G ERα LBD mutant binding to E2.

Figure 4-figure supplement 4: Complete differential HDX perturbation maps comparing the *apo* WT versus *apo* Y537S ERα LBD.

Figure 4-figure supplement 5: Complete differential HDX perturbation maps comparing the *apo* WT versus *apo* D538G ERα LBD.

Figure 4-figure supplement 6: Complete differential HDX perturbation map of WT ERα LBD with SRC3-NRD.

Figure 4-figure supplement 7: Complete differential HDX perturbation map of Y537S ERα LBD with SRC3-NRD.

Figure 4-figure supplement 8: Complete differential HDX perturbation map of D538G ERα LBD with SRC3-NRD.

Figure 4-figure supplement 9: Complete differential HDX perturbation map of WT ERα LBD with E2 and SRC3-NRD.

Figure 4-figure supplement 10: Complete differential HDX perturbation map of Y537S ERα LBD with E2 and SRC3-NRD.

Figure 4-figure supplement 11: Complete differential HDX perturbation map of D538G ERα LBD with E2 and SRC3-NRD.

Figure 4-figure supplement 12: *apo* Y537S x-ray crystal structure (Yellow) (PDB: 2B23) superimposed with WT-E2 complex structure (White) (PDB: 1GWR).

Figure 5: Stabilized D538G agonist state. Superposition stereo-view image of the residues comprising the H11-12 loop (531-537) of monomer A of the D538G-E2 (cyan) overlaid with monomer A of the WT-E2 structure (PDB: 1GWR). E2 is represented as green sticks. Coactivator peptide is shown as light-yellow ribbon.

Figure 5-figure supplement 1: Simulated annealing composite omit maps for the E2 (A) and TOT (B)-bound D538G ERα LBD crystal structures contoured to 1.5σ. E2 and TOT are shown as sticks, helix 12 is highlighted in red, and electron density is shown as a blue cage

Figure 5-figure supplement 2: A) Y537 of the D538G-E2 structure rotates towards solvent and is replaced by a well ordered water molecule (sphere), location of the ligand-binding site is shown with estradiol as green sticks, H11-12 loop and H12 shown as dark-blue. B) Y537 is buried towards Helix 3 in every WT structure, forming a hydrogen bond with N348 (PDB: 1GWR).

Figure 5-figure supplement 3: Density of an unidentified small molecule in the ligand binding site of the *apo* D538G x-ray crystal structure.

Figure 6: Visualization of H11-12 loop dynamics. A) H11-12 loop of WT ERα LBD-E2 complex. B) Superimposing the position of the phenolic oxygen of Y537 at 0.1-ns intervals for *apo* WT (red), WT-E2 (blue), and *apo* D538G mutant (green). C) Mapping the mass density isosurface (0.75, i.e., 25$_{th}$ percentile) of the hydrophobic side chains in the linker region (V533, V534, P535, and L536). D) Side chain packing of the *apo* D538G structure compared to WT-E2. E) Ramachandran analysis of residues 534-538 for the *apo* WT, WT-E2, and *apo* D538G MD simulations. F) Time series of the solvent accessible surface area (SASA) for hydrophobic loop residues (533-536).

Figure 7: Alterations to the D538G and Y537S antagonist conformational states. A) Superposition of monomer A for the 538G-TOT structure with the WT (3ERT). TOT and residues 530-550 of the WT (blue) (PDB: 3ERT), TOT of D538G (green), residues 531-550 (red). B) Predicted conformational alterations in H12 in the Y537S-TOT structure (red) compared to the WT-TOT (blue). C) HDX-MS of the WT-TOT complex for H11 through H12 regions. D) HDX-MS of Y537S-TOT complex for H11 through H12 regions. E) HDX-MS of the D538G-TOT complex for H11 through H12 regions. HDX data is color coded as in 2C. See methods for more details on coloring scheme.

Figure 7-figure supplement 1: Complete differential amide HDX MS map of WT ERα LBD binding to TOT.

Figure 7-figure supplement 2: Complete differential amide HDX MS map of Y537S ERα LBD mutant binding to TOT.

Figure 7-figure supplement 3: Complete differential amide HDX MS map of D538G ERα LBD mutant binding to TOT.

Figure 7-figure supplement 4: Experiment comparison view comparing the differential HDX behavior of *apo* WT ERα LBD in the presence of various ligands or coactivator.

Figure 7-figure supplement 5: Experiment comparison view comparing the differential HDX behavior of *apo* Y537S ERα LBD in the presence of various ligands or coactivator.

Figure 7-figure supplement 6: Experiment comparison view comparing the differential HDX behavior of *apo* D538G ERα LBD in the presence of various ligands or coactivator.

Figure 8: Model of Aberrent ERα Mutant Activity. Upon hormone binding (E2), WT ERα sheds heat-shock/chaperone proteins (HSP), forms head-to-head homodimers, and recruits coactivator (CoA) to become active. By contrast, Y537S or D538G ERα mutants adopt the active conformation in the absence of hormone to recruit CoA and achieve constitutive activity. Additionally, E2 binding may further increase mutant activity.

Table Legends

Table 1: SRC3 NRD and ligand recruitment affinities for the WT and mutant ERα LBDs.

Table 2: Ligand binding affinities.

Table 3: Crystallographic data collection and refinement statistics.

Table 4: Protonation states of histidines for the structure used in MD simulations.

Tables

Table 1

	SRC-3 NRD K_d (nM)
WT apo	*No Recruitment*
Y537S apo	13.6 ± 2.0
D538G apo	151 ± 20
WT-E2	2.67 ± 0.5
Y537S-E2	0.59 ± 0.1
D538G-E2	3.65 ± 0.40
	E2 EC_{50} (nM)
WT	13.8 ± 0.9
Y537S	1.6 ± 1.2
D538G	2.2 ± 0.1
	TOT K_i (nM)
WT	1.82 ± 0.30
Y537S	6.7 ± 0.40
D538G	0.79 ± 0.04

Table 2

	Kd (nM)
WT-E2	0.26 ± 0.13
Y537S-E2	1.43 ± 0.55
D537G-E2	1.30 ± 0.63
	Ki (nM)
WT-TOT	0.337 ± 0.018
Y537S-TOT	2.61 ± 0.60
D538G-TOT	3.42 ± 0.50

Table 3

	ERα LBD D538G Apo	ERα LBD D538G-E2	ERα LBD D538G-4OHT
Data Collection			
Space Group	$P2_1$	$P2_1$	$P2_12_12_1$
a, b, c (Å)	56.14, 82.66, 59.11	56.08, 84.18, 58.37	104.65, 104.65, 191.38
α, β, γ (°)	90.00, 111.05, 90.00	90.00, 108.83, 90.00	90.00, 90.00, 90.00
Resolution Range	55.17-2.24 Å	55.25-1.90	50.00-3.07
Number of Reflections			
(all/unique)	91,607/24,107	169,519/40,361	60,232/9,874
I/σ (highest resolution)	2.37	2.36	1.70
R_{merge}	11.4	7.3	11.4
Completeness (%)	98.9	99.3	96.7
Redundancy	3.8	4.2	6.1
Refinement			
Rwork/Rfree	19.8/24.9	17.9/21.4	21.6/28.3
No. Residues/Chain			
ERα LBD D538G	241	242	216
GRIP Peptide	6	6	0
Water	16	44	2
Ligand	0	1	1
RMSD			
Bond lengths (Å)	0.015	0.0170	0.0128
Bond angles (°)	1.76	1.5441	1.5356
Chiral volume	0.1117	0.1267	0.1036
Ramachandran plot statistics			
Preferred number (%)	428 (96.40%)	443 (98.88%)	1,563 (95.42%)
Additional allowed (%)	3.60 (3.6%)	5 (1.12 %)	75 (4.58%)
Outliers (%)	0	0	0

989 Table 4

HIS Residue Number	Monomer A	Monomer B
356	HSE	HSD
373	HSD	HSE
377	HSE	HSD
398	HSP	HSP
474	HSE	HSE
476	HSE	HSE
488	HSE	HSE
501	HSD	HSE
513	HSD	HSD
516	HSE	HSE
524	HSE	HSE
547	HSE	HSE

990

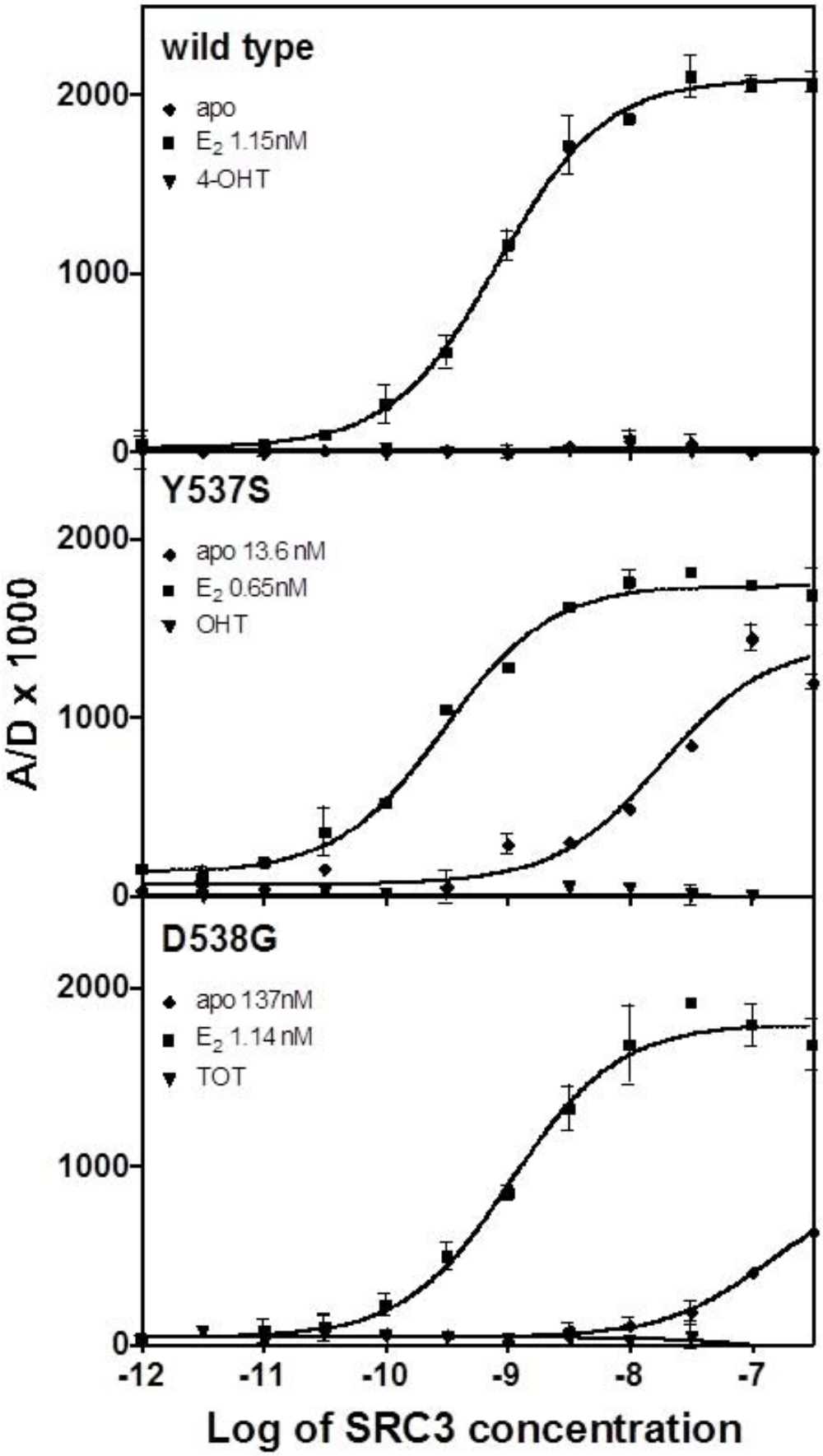
wild type
apo
E2 1.15nM
4-OHT
Y537S
apo 13.6 nM
E2 0.65nM
OHT
D538G
apo 137nM
E2 1.14 nM
TOT
2000
1000
0
A/D x 1000
-12
-11
-10
-9
-8
-7
Log of SRC3 concentration

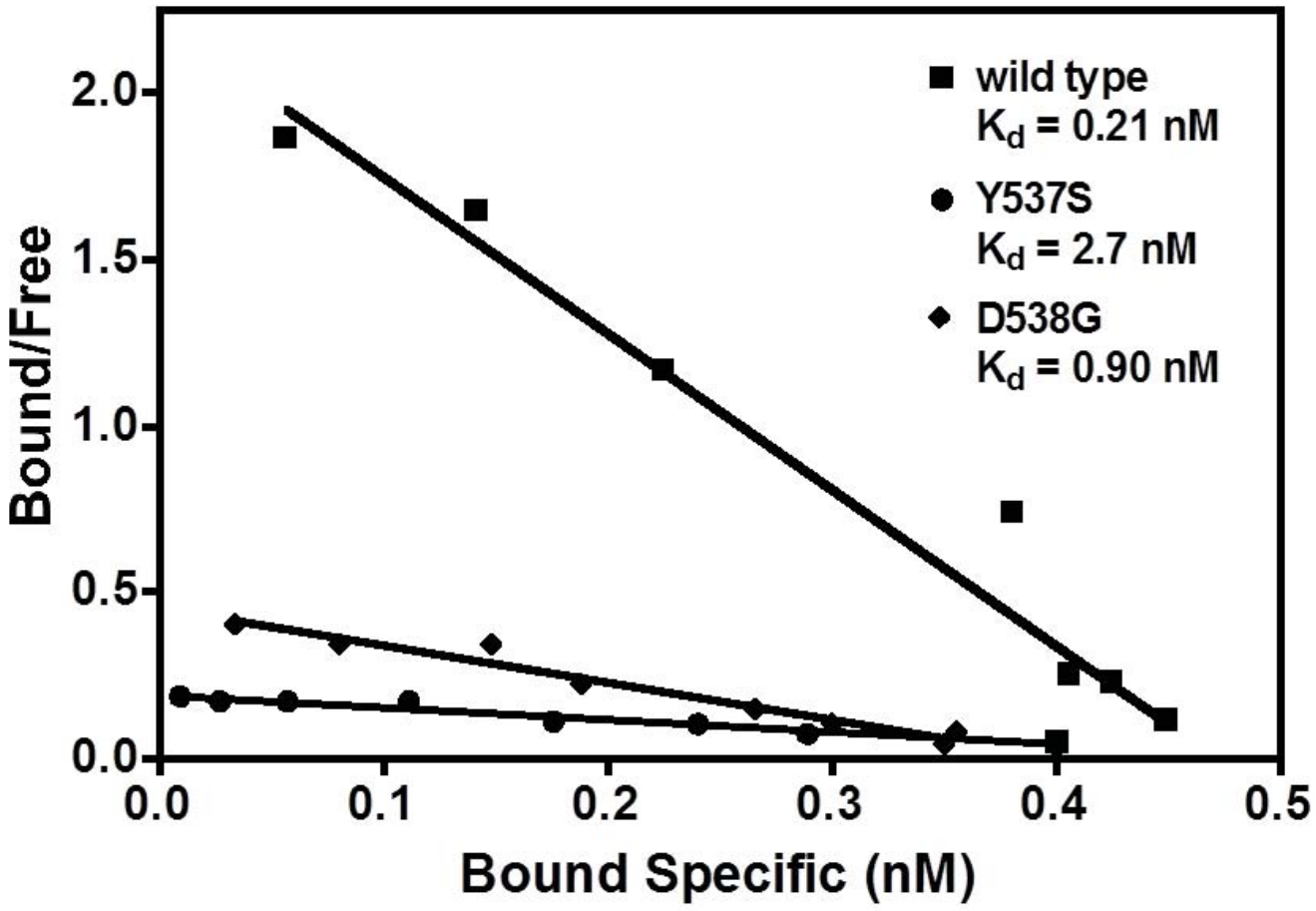
wild type
K_d = 0.21 nM
Y537S
K_d = 2.7 nM
D538G
K_d = 0.90 nM
Bound/Free
2.0
1.5
1.0
0.5
0.0
0.0
0.1
0.2
0.3
0.4
0.5
Bound Specific (nM)

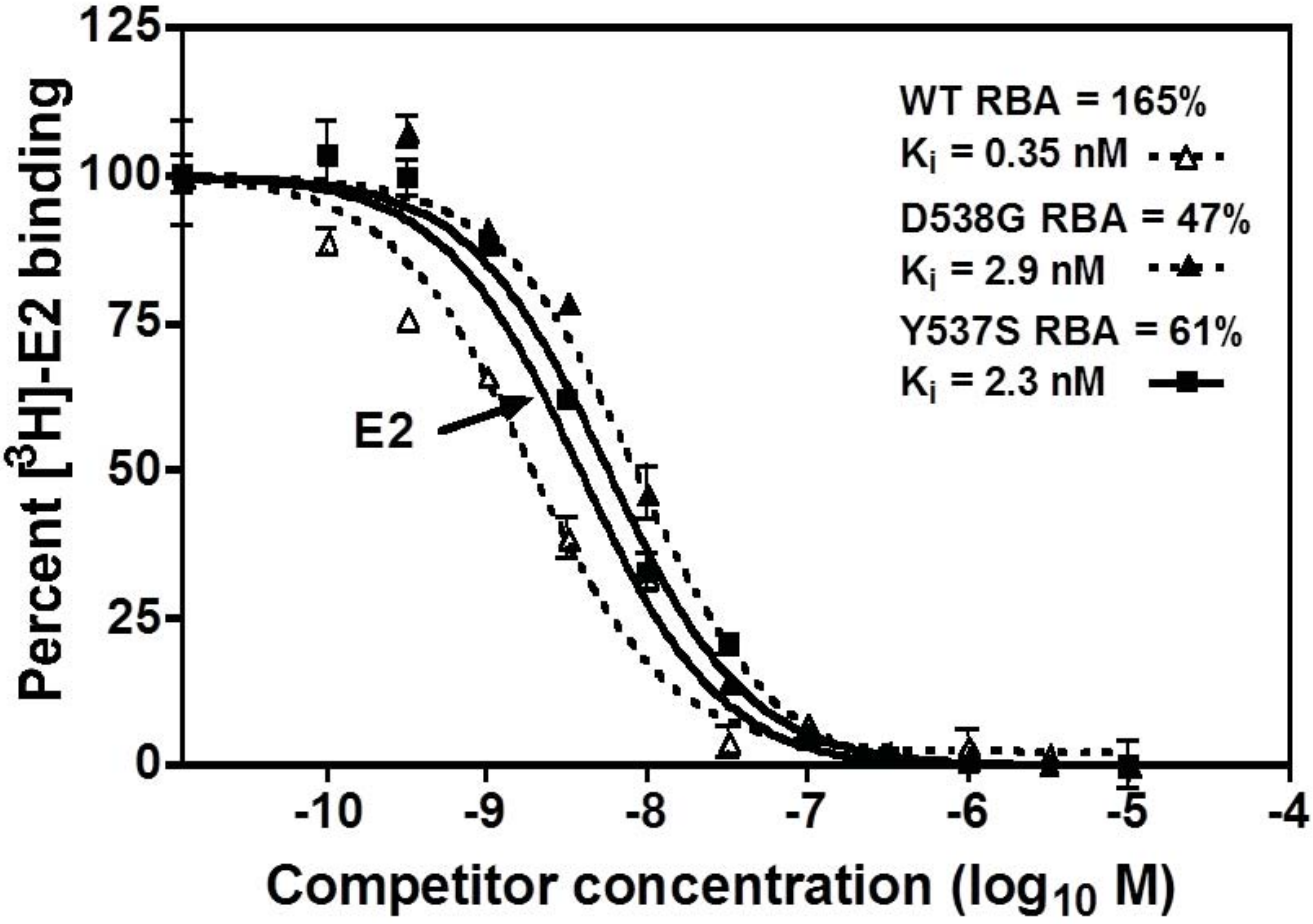
125
100
75
50
25
0
Percent [3H]-E2 binding
-10
-9
-8
-7
-6
-5
-4
Competitor concentration (log10 M)
WT RBA = 165%
Ki = 0.35 nM
D538G RBA = 47%
Ki = 2.9 nM
Y537S RBA = 61%
Ki = 2.3 nM
E2

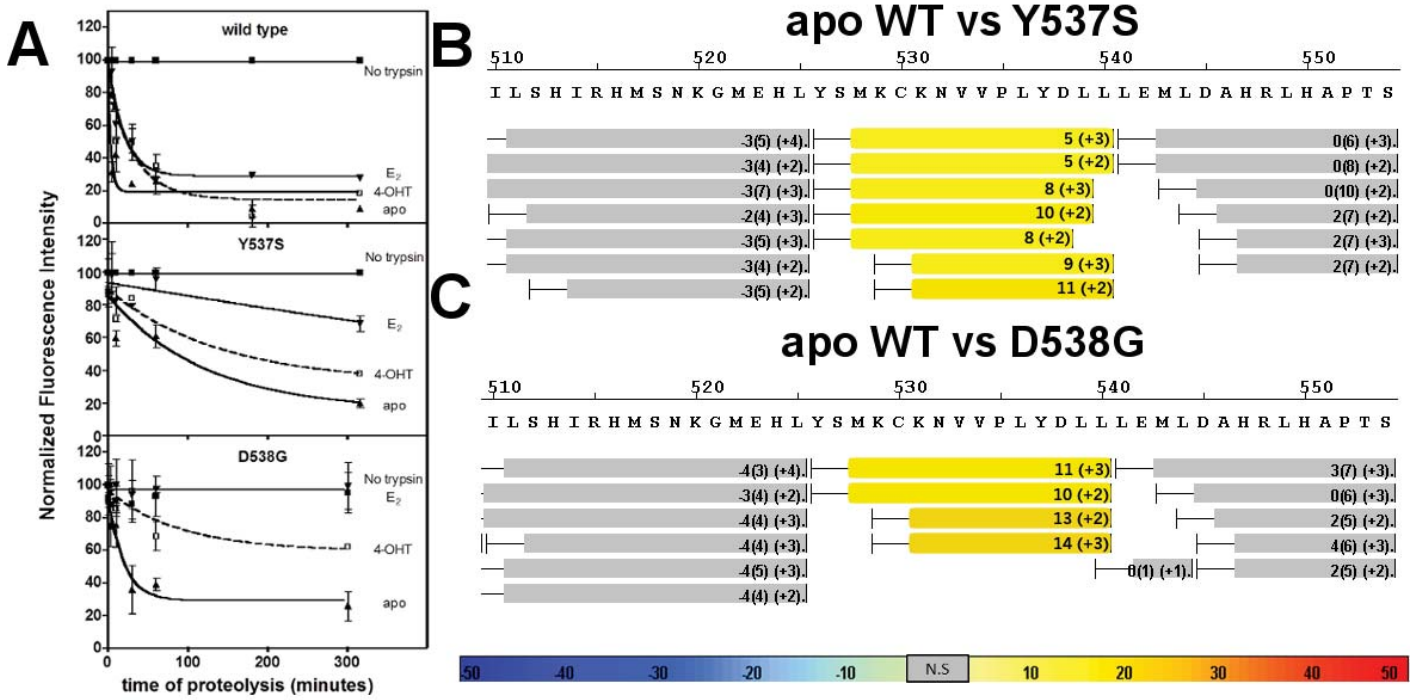
A
wild type
No trypsin
E2
4-OHT
apo
Y537S
No trypsin
E2
4-OHT
apo
D538G
No trypsin
E2
4-OHT
apo
Normalized Fluorescence Intensity
time of proteolysis (minutes)
B
apo WT vs Y537S
510
520
530
540
550
I L S H I R H M S N K G M E H L Y S M K C K N V V P L Y D L L L E M L D A H R L H A P T S
-3(5) (+4).
5 (+3)
0(6) (+3).
-3(4) (+2).
5 (+2)
0(8) (+2).
-3(7) (+3).
8 (+3)
0(10) (+2).
-2(4) (+3).
10 (+2)
2(7) (+2).
-3(5) (+3).
8 (+2)
2(7) (+3).
-3(4) (+2).
9 (+3)
2(7) (+2).
-3(5) (+2).
11 (+2)
C
apo WT vs D538G
510
520
530
540
550
I L S H I R H M S N K G M E H L Y S M K C K N V V P L Y D L L L E M L D A H R L H A P T S
-4(3) (+4).
11 (+3)
3(7) (+3).
-3(4) (+2).
10 (+2)
0(6) (+3).
-4(4) (+3).
13 (+2)
2(5) (+2).
-4(4) (+3).
14 (+3)
4(6) (+3).
-4(5) (+3).
0(1) (+1).
2(5) (+2).
-4(4) (+2).
-50
-40
-30
-20
-10
N.S
10
20
30
40
50

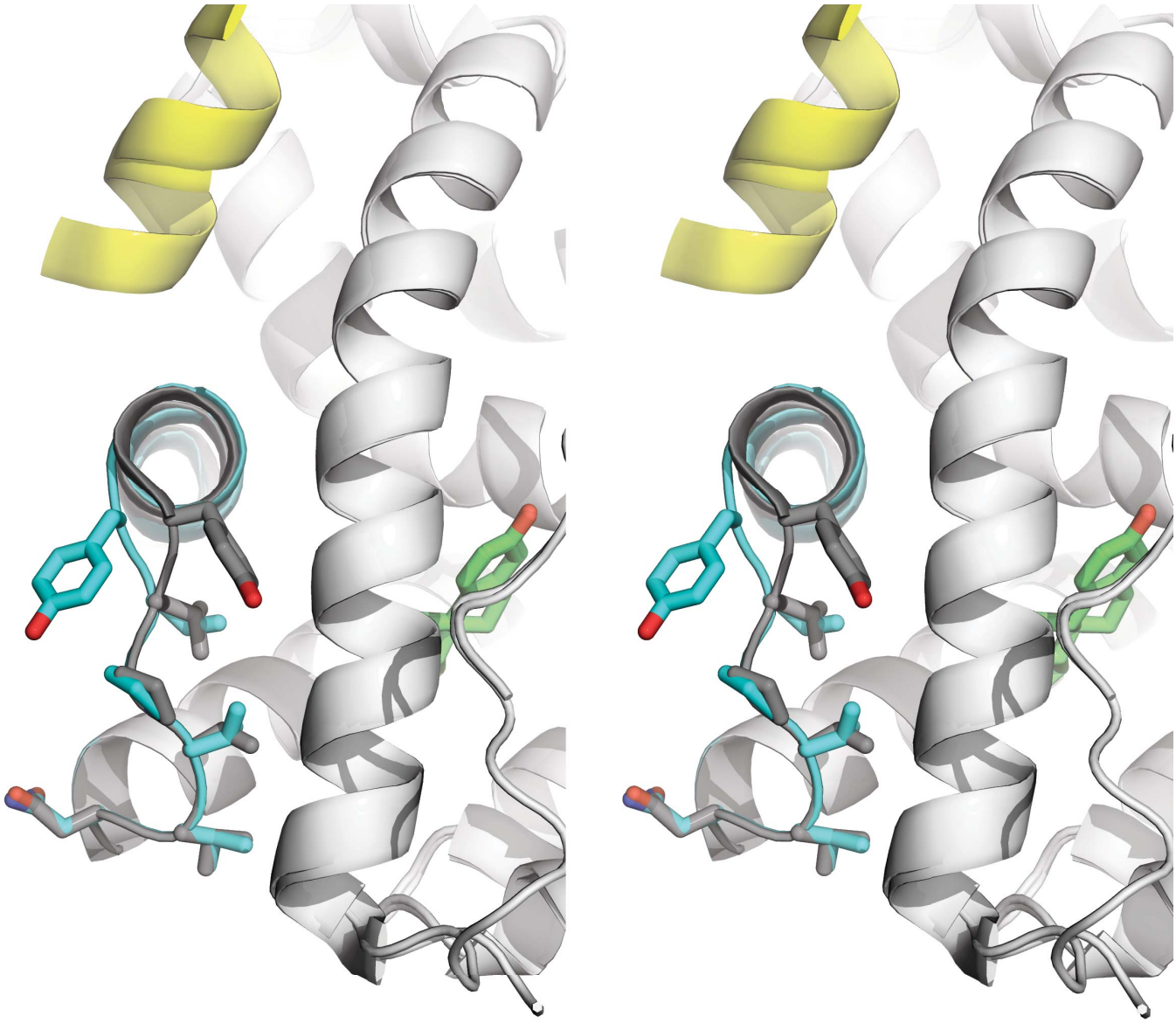

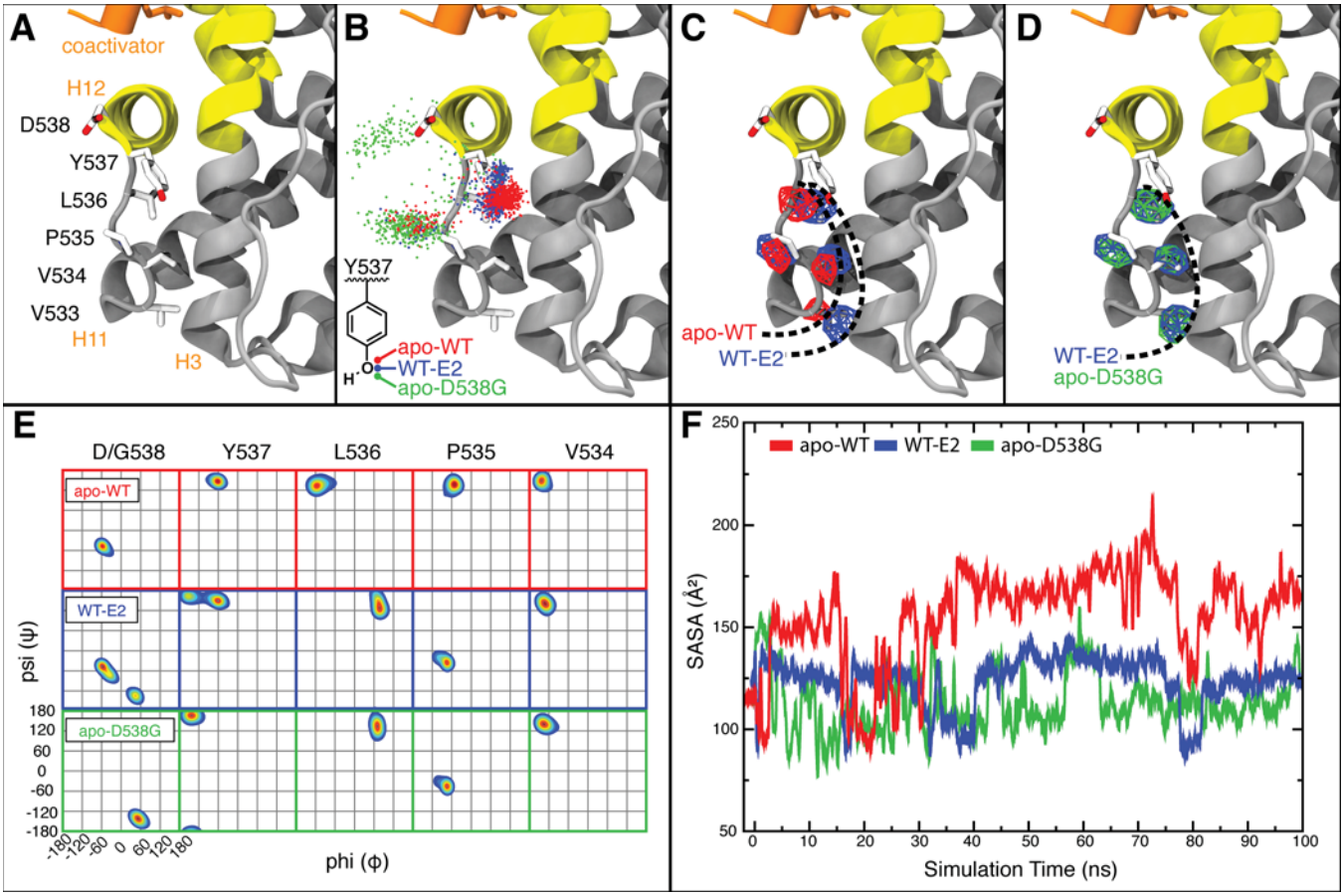
A
coactivator
H12
D538
Y537
L536
P535
V534
V533
H11
H3
B
Y537
apo-WT
WT-E2
apo-D538G
C
apo-WT
WT-E2
D
WT-E2
apo-D538G
E
D/G538
Y537
L536
P535
V534
apo-WT
WT-E2
apo-D538G
psi (ψ)
phi (ϕ)
F
apo-WT
WT-E2
apo-D538G
SASA (Å²)
Simulation Time (ns)

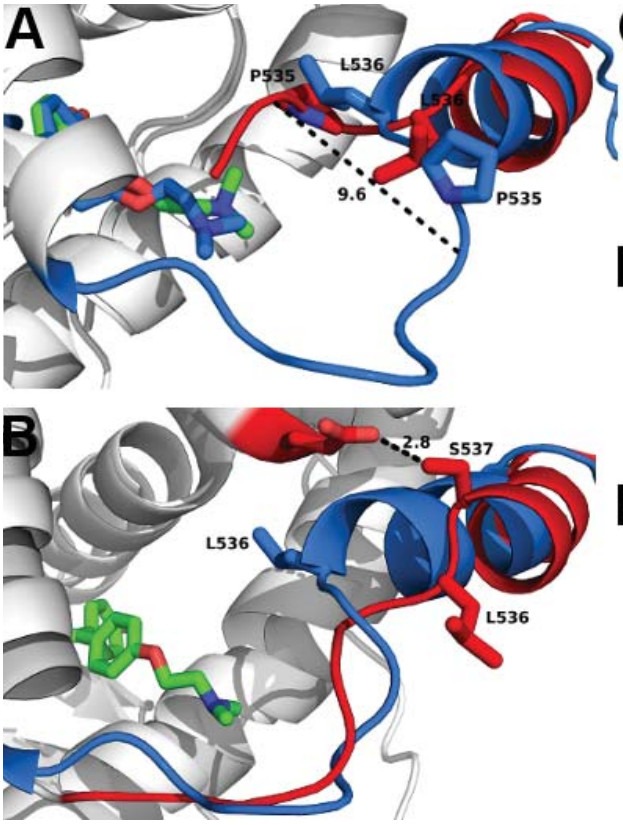
A
P535
L536
L536
9.6
P535
B
2.8
S537
L536
L536

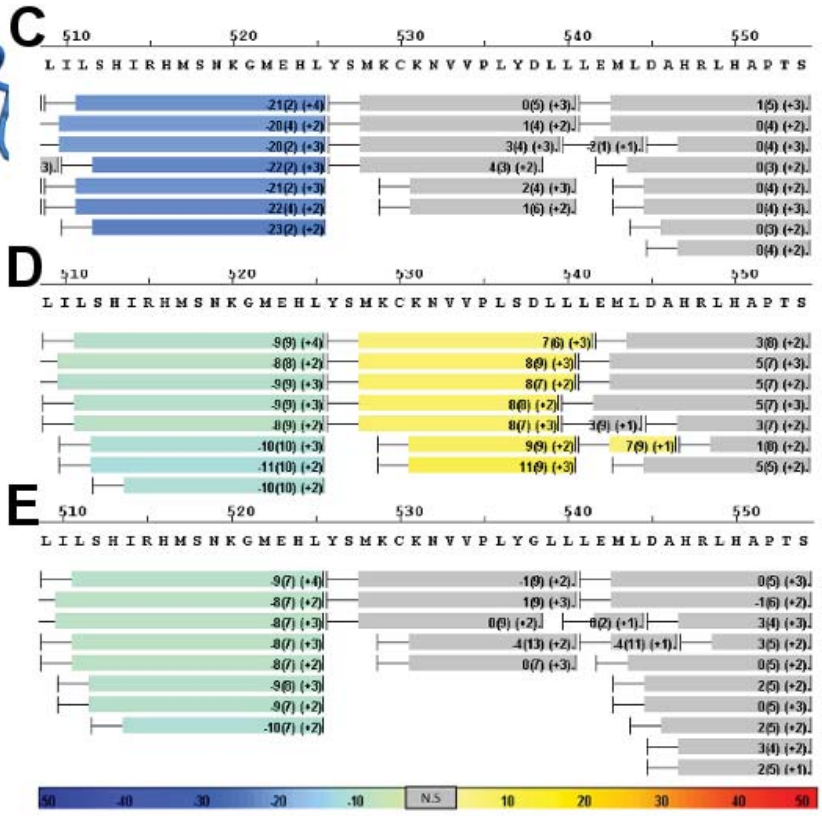
C
510
520
530
540
550
L I L S H I R H M S N K G M E H L Y S M K C K N V V P L Y D L L L E M L D A H R L H A P T S
D
L I L S H I R H M S N K G M E H L Y S M K C K N V V P L S D L L L E M L D A H R L H A P T S
E
L I L S H I R H M S N K G M E H L Y S M K C K N V V P L Y G L L L E M L D A H R L H A P T S
N.S

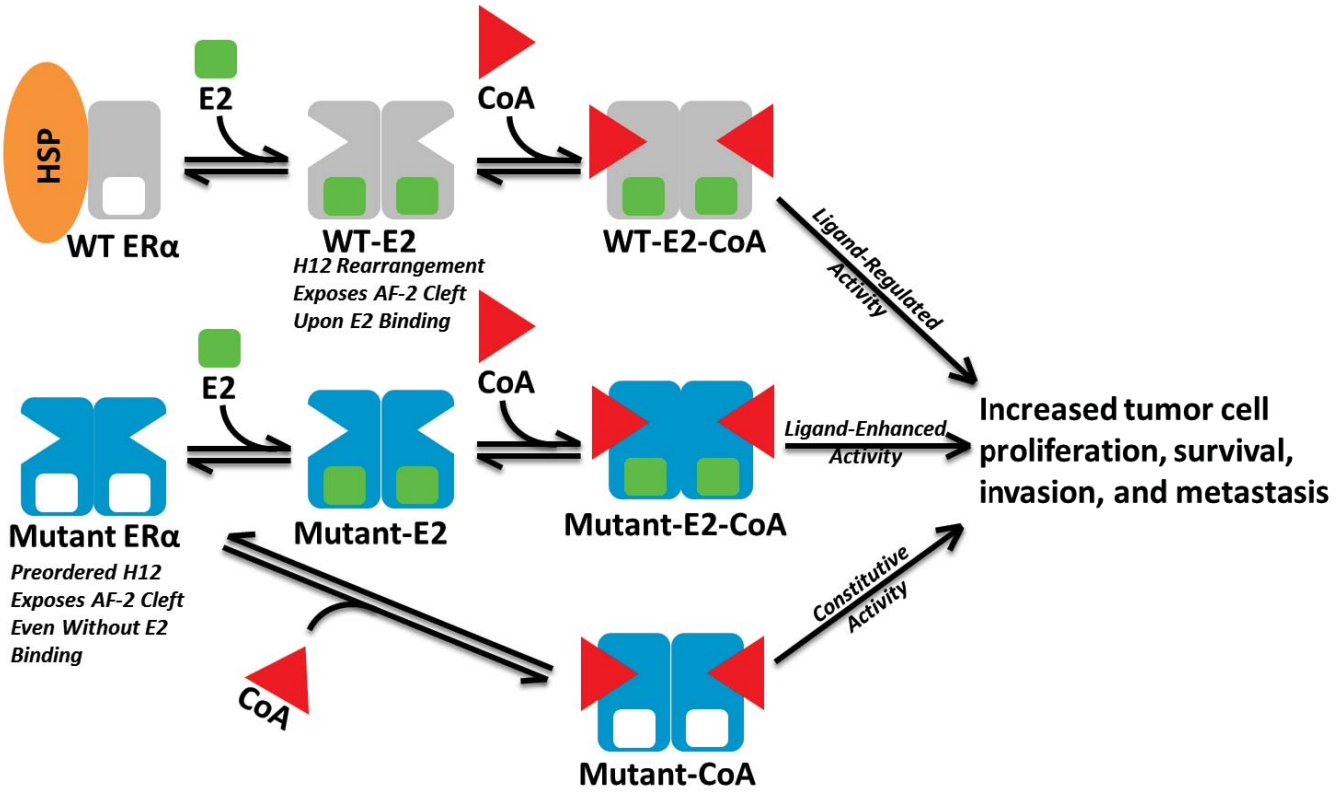
HSP
WT ERα
E2
WT-E2
H12 Rearrangement
Exposes AF-2 Cleft
Upon E2 Binding
CoA
WT-E2-CoA
Ligand-Regulated
Activity
Mutant ERα
Preordered H12
Exposes AF-2 Cleft
Even Without E2
Binding
E2
Mutant-E2
CoA
Mutant-E2-CoA
Ligand-Enhanced
Activity
Increased tumor cell
proliferation, survival,
invasion, and metastasis
CoA
Mutant-CoA
Constitutive
Activity